NAVAL POSTGRADUATE SCHOOL

MONTEREY, CALIFORNIA

THESIS

A STUDY OF THE CORRELATION BETWEEN DISLOCATIONS AND DIFFUSION LENGTH IN In$_{49}$Ga$_{51}$P SOLAR CELLS

by

Scott Edward Williams

December 2008

Thesis Advisor:	Nancy Haegel
Second Reader:	Clyde Scandrett

Approved for public release; distribution is unlimited

THIS PAGE INTENTIONALLY LEFT BLANK

1. AGENCY USE ONLY *(Leave blank)*	2. REPORT DATE December 2008	3. REPORT TYPE AND DATES COVERED Master's Thesis	

4. TITLE AND SUBTITLE A Study of the Correlation Between Dislocations and Diffusion Length in $In_{49}Ga_{51}P$	5. FUNDING NUMBERS
6. AUTHOR(S) Scott Edward Williams	

7. PERFORMING ORGANIZATION NAME(S) AND ADDRESS(ES) Naval Postgraduate School Monterey, CA 93943-5000	8. PERFORMING ORGANIZATION REPORT NUMBER

9. SPONSORING /MONITORING AGENCY NAME(S) AND ADDRESS(ES) National Science Foundation Division of Materials Research (DMR)	10. SPONSORING/MONITORING AGENCY REPORT NUMBER

11. SUPPLEMENTARY NOTES The views expressed in this thesis are those of the author and do not reflect the official policy or position of the Department of Defense or the U.S. Government.

12a. DISTRIBUTION / AVAILABILITY STATEMENT Approved for public release; distribution is unlimited	12b. DISTRIBUTION CODE

13. ABSTRACT (maximum 200 words)

A quantitative, contact-free method for extracting minority carrier diffusion length is used to measure the relatively small variations in diffusion length associated with dislocation bands in mismatched epitaxy in the p-type region of a two dimensional heterostructure of a triple junction (InGaP/GaAs/Ge) solar cell sample. These measurements are taken using the line scan mode of a Scanning Electron Microscope coupled with an optical microscope.

This technique allowed the variations in diffusion length in the $In_{49}Ga_{51}P$ sample to be measured to within 0.1 microns. Also, the variations were not random but varied spatially with respect to the light and dark cathodoluminescence bands on the sample. However, there is an inverse relationship between the maximum luminescent intensity and the diffusion length. Since the radiative lifetime and non-radiative lifetime are on the same order of magnitude, a relationship between the maximum luminescent intensity and minority carrier diffusion length to the lifetimes were derived. With the radiative lifetime inversely dependent on the free hole concentration, a simulation was conducted to qualitatively reproduce the relationship between luminescent intensity and minority carrier diffusion length.

The model simulated the non-radiative lifetime and free hole concentration decreasing across dislocation bands. This described the behavior of the non-radiative lifetime due to defect states associated with the dislocations. It also qualitatively illustrated the increase in radiative lifetime if the free hole concentration is reduced due to variations in Fermi level. Therefore, the simulation qualitatively described the spatial behavior of the diffusion length due to the presence of dislocations and reproduced the experimental anti-correlation between the diffusion length and maximum luminescent intensity. Areas of further research are offered to expand this work to other triple junction solar cell materials to include effects of lattice mismatched materials, varying mole concentrations, atomic ordering, and doping concentration.

14. SUBJECT TERMS Triple junction solar cells, InGaP, solar cells, semiconductor, diffusion length, transport imaging, cathodoluminescence, dislocations, radiative lifetime, non-radiative lifetime, free hole concentration	15. NUMBER OF PAGES 111
	16. PRICE CODE

17. SECURITY CLASSIFICATION OF REPORT Unclassified	18. SECURITY CLASSIFICATION OF THIS PAGE Unclassified	19. SECURITY CLASSIFICATION OF ABSTRACT Unclassified	20. LIMITATION OF ABSTRACT UU

THIS PAGE INTENTIONALLY LEFT BLANK

A STUDY OF THE CORRELATION BETWEEN DISLOCATION AND DIFFUSION LENGTH IN In$_{49}$Ga$_{51}$P SOLAR CELLS

Scott E. Williams
Lieutenant, United States Navy
B.S., United States Naval Academy, 2001

Submitted in partial fulfillment of the
requirements for the degree of

MASTER OF SCIENCE IN PHYSICS

from the

NAVAL POSTGRADUATE SCHOOL
December 2008

Author: Scott Edward Williams

Approved by: Nancy M. Haegel
                 Thesis Advisor

                 Clyde Scandrett
                 Second Reader

                 James H. Luscombe
                 Chairman, Department of Physics

THIS PAGE INTENTIONALLY LEFT BLANK

ABSTRACT

A quantitative, contact-free method for extracting minority carrier diffusion length is used to measure the relatively small variations in diffusion length associated with dislocation bands in mismatched epitaxy in the p-type region of a two dimensional heterostructure of a triple junction (InGaP/GaAs/Ge) solar cell sample. These measurements are taken using the line scan mode of a Scanning Electron Microscope coupled with an optical microscope.

This technique allowed the variations in diffusion length in the $In_{49}Ga_{51}P$ sample to be measured to within 0.1 microns. Also, the variations were not random but varied spatially with respect to the light and dark cathodoluminescence bands on the sample. However, there is an inverse relationship between the maximum luminescent intensity and the diffusion length. Since the radiative lifetime and non-radiative lifetime are on the same order of magnitude, a relationship between the maximum luminescent intensity and minority carrier diffusion length to the lifetimes were derived. With the radiative lifetime inversely dependent on the free hole concentration, a simulation was conducted to qualitatively reproduce the relationship between luminescent intensity and minority carrier diffusion length.

The model simulated the non-radiative lifetime and free hole concentration decreasing across dislocation bands. This described the behavior of the non-radiative lifetime due to defect states associated with the dislocations. It also qualitatively illustrated the increase in radiative lifetime if the free hole concentration is reduced due to variations in Fermi level. Therefore, the simulation qualitatively described the spatial behavior of the diffusion length due to the presence of dislocations and reproduced the experimental anti-correlation between the diffusion length and maximum luminescent intensity. Areas of further research are offered to expand this work to other triple junction solar cell materials to include effects of lattice mismatched materials, varying mole concentrations, atomic ordering, and doping concentration.

THIS PAGE INTENTIONALLY LEFT BLANK

TABLE OF CONTENTS

LIST OF FIGURES

THIS PAGE INTENTIONALLY LEFT BLANK

LIST OF TABLES

THIS PAGE INTENTIONALLY LEFT BLANK

ACKNOWLEDGMENTS

First of all I want to thank the Lord for all the blessings that he has bestowed upon me and my family. He has provided me with the tools and the talent to follow this path, and it is for His glory that I do this work.

My sincere thanks and appreciation go out to the folks at Spectrolab, Inc. Without their knowledge, expertise, and solar cell samples, this work could not have been accomplished. I would also like to extend a special thank you to Dr. Pete Crooker, who helped me understand various aspects of the simulation I was developing and assisted me in preparation for my presentation of this material. I would also like to thank my co-advisor, Dr. Clyde Scandrett for taking time out of his busy schedule to help me better understand the intricate details of the mathematics behind the physics.

And of course a special thank you goes to my advisor, Dr. Nancy Haegel. I appreciate all the time and dedication she gave to teaching this engineer how to think like a physicist. Her patience, understanding, and guidance throughout this whole process were invaluable in helping me pull all of this together and paved the way for me to further my physics education. Her enthusiasm for research is unparalleled and her excitement in explaining new and unexpected experimental results motivated me to work just that much harder. I just can't thank her enough and will always recognize this as the start of my scientific career.

And where would I be if it were not for the love and support of my wife, Kelly. While I was trying to solve the mysteries of the solar cell world, she had the most difficult job of all and that was of taking care of the household and raising our children. I just want to say that I love you more than you know and I appreciate all that you did and your patience while I was here studying here at NPS. In addition, I also want to thank my children, Isabella, Ethan, and Lucas. They are the joy of my life and I appreciate their patience with me during this busy time.

THIS PAGE INTENTIONALLY LEFT BLANK

I.   INTRODUCTION

A.   MAPPING DIFFUSION LENGTH VARIATION IN SOLAR CELL MATERIALS

With the rising concerns for global warming, coupled with high oil prices and increasing government support, the need for low cost, high efficiency renewable energy sources is at an all time high. The energy generated from natural resources such as sunlight, wind, rain, tides, and geothermal heat are some examples of renewable energy sources. In 2006, about 18 percent of global final energy consumption came from renewables with approximately one percent from photovoltaic technology [1], [2]. Photovoltaic devices employ the use of solar cells to collect sunlight and then convert the light into electricity. The fact that only 0.6 percent of renewable energy was generated from solar cells is important because solar radiation along with several other secondary solar resources account for 99.97 percent of the available energy on Earth [3], [4]. The total solar energy absorbed by Earth's atmosphere, oceans, and land masses is approximately 3850 zettajoules (ZJ) per year [5]. In 2002, this was more energy in one hour than the world used in one year [6]. The amount of solar energy reaching the surface of the planet is so vast that in one year it is about twice as much as will ever be obtained from all the Earth's non-renewable resources of coal, oil, natural gas, and mined uranium combined. Unfortunately, to harness this vast well of energy, improvements to current space and terrestrial solar cell technology must be made.

Terrestrial solar cell technology is used in a variety of applications such as architecture, urban planning, agriculture, horticulture, heating, and cooling. Despite all of these uses, there are currently three major limitations associated with terrestrial solar cells; low power conversion efficiency, high cost per watt-hour and the area required for the cells and associated equipment. Current photovoltaic ground modules in use have only achieved 10 percent efficiency, though higher efficiencies up to 16.5 percent have been produced at the national Renewable Energy Laboratory and Boeing has reported achieving 22 percent efficiency, but none of these have been implemented commercially

[7]. In addition an installed system costs about 4-5 $/watt. This is much more expensive than today's rates for conventional power sources, which are on average 0.12 $/watt [2]. Finally, due to the relatively low efficiency of the solar cells, large areas of land, tens of thousands of square miles, are required to build enough photovoltaic modules to collect enough light, convert and store the needed amount of power, and distribute the power to the required number of homes, businesses, and other customers. Therefore, according to the Department of Energy and the Energy Foundation, in order for terrestrial solar cells to be a competitive technology for energy production, the photovoltaic modules must convert electricity with at least 14 percent efficiency, and systems would have to be installed at $1.20 per watt of capacity. Progress is clearly needed on the ground.

Space solar cell technology has long been a focus of cutting-edge, high efficiency devices. Currently, there are three major issues regarding space solar cells; onboard power requirements, mass, and cost. As the operational demand increases for satellites to become more versatile and multi-mission, more equipment is being designed into the standard buses. In addition, customers are demanding satellite response times to decrease as well. In order to meet the myriad number of required missions in the allotted time more complex imagers have been designed, higher frequency communication antennas are being installed, more powerful computers are interconnected, and faster attitude control equipment has been added. All of this equipment can require hundreds of watts of power at once. Storage units such as batteries can not always provide this power before they run out of charge. In addition, storage units can be massive and some contain radioactive material required for long term power generation. Therefore, thin layered, high efficiency solar cells appear to be the most promising option for space applications. The current space qualified solar cells have a reported energy conversion efficiency of 28.5 percent, however, experimentally efficiencies have been reported as high as 40 percent for solar cells using a concentrator. The next generation of solar cells with proven efficiencies above 30 percent is currently too expensive for use on satellites which are already experiencing cost overruns. Unfortunately, the concentrator adds additional cost and mass making it a less desirable option for satellite designs. Solar arrays can be directed towards the sun on a continuous basis, but controllers to do so add mass,

2

complexity, and cost. A solution to these complex problems is the development of a thin film, high efficiency solar cell that can be used either terrestrially or in space. The key to developing such a solar cell motivates further research and development. One aspect of that research involves study of the properties of the materials used and how they interact with one another.

Currently there are many different solar cell, or photovoltaic device, configurations with a variety of materials used for various applications. The most efficient configuration is the p-n multi-junction photovoltaic cell. Semiconductors that have an excess of free electrons are referred to as n-type materials, and semiconductors that have an excess of holes are referred to as p-type materials. In n-type materials, holes are referred to as the minority carriers while in p-types, the minority carriers are electrons. One of the key physical properties of such materials is the diffusion length. When n-doped and p-doped pieces of semiconductor are placed together to form a p-n junction, electrons diffuse into the p-side and holes diffuse into the n-side. Electrons exiting an n-region near the junction leave behind exposed positively charged donor ions. Similarly, holes exiting a p-region near the junction expose negatively charged acceptor ions. Within the p-type region, the minority carriers (electrons) will recombine with holes. An identical process occurs for the injected holes within an n-type region. After all of the excess electrons and holes have recombined in an area, there are no longer any mobile carriers and it is referred to as a depletion region [8], [9], [10]. In addition, charged ions are left behind which create an electric field. Electrons, which are the minority charge carriers in a p-type region, must have a large enough diffusion length to diffuse into a depletion region where they are forced into the n-type region by the electric field [10]. In the collection of photogenerated charges, a photon will be absorbed at the junction if its energy is equal to or greater than the material's energy band gap. Electron-hole pairs are created and diffused from regions of high electron concentration to regions of low concentration. The transport and collection of the charge carriers determine the overall performance of the solar cell. If the diffusion length is not of sufficient size then the electron may be lost to recombination and overall performance will decrease.

3

These p-n junctions are used in series in the production of multi-junction photovoltaic cells to gain efficiency. They consist of multiple thin films produced using molecular beam epitaxy or metalorganic vapor phase epitaxy. Each type of semiconductor material used in a multi-junction solar cell has its own characteristic band gap energy. This will allow the solar cell to absorb light more efficiently over a spectrum of wavelengths, so that the semiconductor layers are able to absorb a large fraction of the solar energy to generate electricity. The ability to optimize the respective band gaps of the various junctions is hampered by the requirement that each layer must be lattice matched to all other layers [11].

Because of lattice matching another important parameter in the production of semiconductors is the lattice constant of the crystal structures. The lattice constant is the size of a unit cell in a crystalline material. In epitaxial growth, which is the method of depositing a monocrystalline film on a monocrystalline substrate, the variation in lattice constant is a measure of the structural compatibility between different materials. Lattice constant matching is important for growth of thin layers of materials on other materials. When the constants differ, strains are introduced into the layer, which prevent defect-free epitaxial growth of thicker layers [9], [10], [12]. Matching lattice structures between two different semiconductor materials allows formation of a region of band gap variation in the device without introducing a change in crystal structure and thereby minimizes film stress. Unfortunately, the lattice match is often not perfect and the film stress cannot be totally eliminated so dislocations, or crystallographic defects, are formed within the crystal structure at the boundaries of each junction.

Dislocations are of particular interest because of their degrading effect on the carrier lifetime and related luminescence of the semiconductor material. Dislocations are always present in multi-junction cells due to the small variations in lattice constants that despite all best efforts remain slightly mismatched. These in turn influence the radiative and non-radiative minority carrier lifetimes. It has been shown that the luminescence from the material can be used to determine diffusion lengths of minority charge carriers, which in turn is related to the effective minority carrier lifetime. Investigating the relationship between the magnitudes of the luminescent intensity at the dislocations, the

4

associated diffusion length, and the mechanisms that may be underlying this relationship are key to further understanding the physics of multi-layer semiconductor systems and optimizing performance.

B. PURPOSE OF THESIS

The goal of this thesis is to develop the ability to measure the relatively small (1-7 percent) variations in diffusion length associated with dislocation bands in mismatched epitaxy, and provided the variations are measureable, to determine the relationship between variations in diffusion length and luminescent intensity. A technique was developed to extract the minority charge carrier diffusion lengths from a one dimensional analysis using position versus intensity and will be applied to determine the diffusion length of minority charge carriers in the p-type region of a 2D heterostructure of a triple junction (InGaP/GaAs/Ge) solar cell sample. The intensity variation of the multiple dislocation bands within the InGaP sample were measured using the line scan mode of the Scanning Electron Microscope (SEM) and a charge coupled device (CCD) camera in the Physics department at the Naval Postgraduate School (NPS).

C. MILITARY RELEVANCE

The military's reliance on space assets and the need for operational responsive space has caused an increasing demand in finding more efficient, cost effective power source technologies to employ on its satellites. The request from military commanders to have more information in a shorter period of time has increased the government's willingness to invest money into developing smaller, more diverse satellites. This means that the satellites will have more functionality; but must be small and compact in order to reduce weight and remain inexpensive. Increased functionality unfortunately means that more equipment must be included into the standard bus. The additional equipment means that the power requirements must increase. The current sources of power generation, batteries, fuel cells, and radioisotope thermal generators, are complex, costly, and not very reliable over long periods of time. Recently developed high efficiency solar cells require three or more junctions and additional concentrator mechanisms, which add mass

and complexity to the system. Such metamorphic solar cells are costly to produce and are unacceptable for satellite applications. In addition to space requirements the high cost of energy and concerns for the terrestrial environment have forced the military and industry to increase its search for clean, cheap alternative forms of energy. While the metamorphic solar cell mentioned previously is a promising solution, it is not currently economical to produce. One key to developing a solar cell material that is cost effective and provides more efficient energy conversion is by understanding the internal mechanisms that affect charge transport at the various defect sites within the crystalline structure. This understanding could help in developing new crystal growth techniques that will further minimize the effects due to the difference in lattice constants between the heterostructures and substrates. More efficient charge transport results in greater power generation, reducing the number of cells per panel, thereby reducing weight and volume requirements while improving cost effectiveness.

D. THESIS OVERVIEW

Chapter I provides an introduction to the thesis and explains the importance of a material's diffusion length in charge transport. It also describes the lattice constant associated with a particular solar cell crystal lattice structure and how dislocations are formed due to lattice mismatching. Chapter I continues to introduce how the dislocations affect the photogeneration intensity and the minority carrier lifetime. The purpose of the thesis and a discussion of the military relevance are also presented. A review of solar cell technology, with emphasis on triple junction cells and an explanation of dislocations and lattice mismatch is given in Chapter II. Additionally, charge carriers in semiconductors, luminescence in semiconductors, and diffusion, mobility, and lifetime of charge carriers are reviewed.

Chapter III introduces the experimental approach and apparatus used for one dimensional transport imaging and describes the equipment used. The experimental methodologies to extract diffusion length are also presented. Chapter IV reviews the slope analysis estimation technique for the diffusion length and details initial observations from the graphs of luminescence variation and diffusion length extracted

from the line scan data. It describes the correlation between the luminescence variation and diffusion length associated with dislocation bands. This is followed by a derivation and explanation of the observed results. Finally, Chapter V summarizes the results and suggests further areas of research.

THIS PAGE INTENTIONALLY LEFT BLANK

II.   ONE DIMENSIONAL TRANSPORT IMAGING THEORY AND MODELING

A.   TRIPLE JUNCTION SOLAR CELLS

The transport imaging technique applied in this thesis experimentally allows the extraction of the diffusion lengths of minority charge carriers in luminescent semiconductor materials. The focus of this work is on the p-type InGaP layers of a triple junction solar cell sample of InGaP/GaAs/Ge. In a single band gap solar cell, efficiency is limited by an inability to convert the broad range of photon energy from in the solar spectrum. Photons with energy above or below the band gap energy of a cell material are lost; either passing through the cell or generating heat within the material. Only the energy necessary to generate the hole-electron pair is utilized, and the remaining energy is lost, thus reducing the efficiency [13].

The goal of a multi-junction solar cell is to take advantage of the different characteristic band gap energies of semiconductor alloys in order to use more of the solar spectrum. By using different group III-V semiconductor alloys, the band gap of each layer may be tuned to optimally absorb a specific range of the solar electromagnetic spectrum [13]. The material with the highest band gap will be on top and absorb the photons with the highest energy. The photons that have energy less than the band gap energy of the first layer will pass through to the next layers and be absorbed there. Figure 1 shows the absorption efficiency of each layer of the multi-junction cell, and the overall absorption efficiency of the solar cell as a function of solar spectrum wavelength.
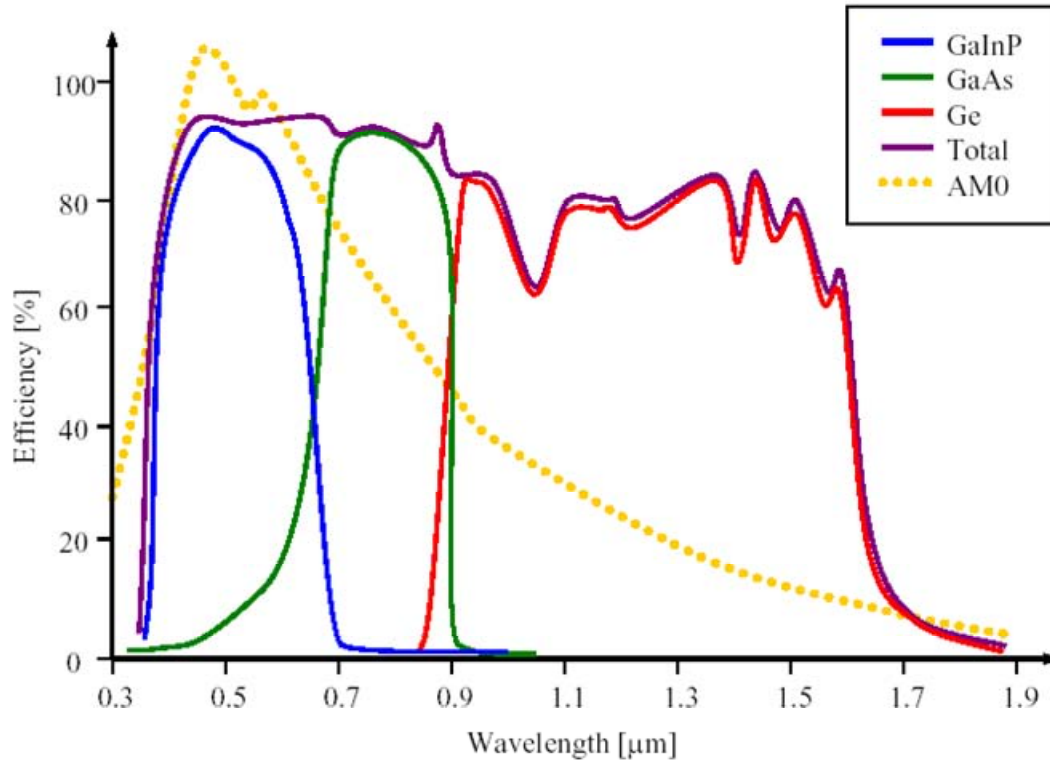
Figure 1.   Triple-Junction Solar Cell Absorption Efficiency [From: 15].

The Air Mass Zero (AMO) solar constant is the typical absorption efficiency that is common in space. It can be seen in Figure 1 that the solar spectrum is more efficiently used by the triple junction cell vice a solar cell that is only single or dual junction [14].

Figure 2 shows a typical high efficiency triple-junction solar cell currently in use.
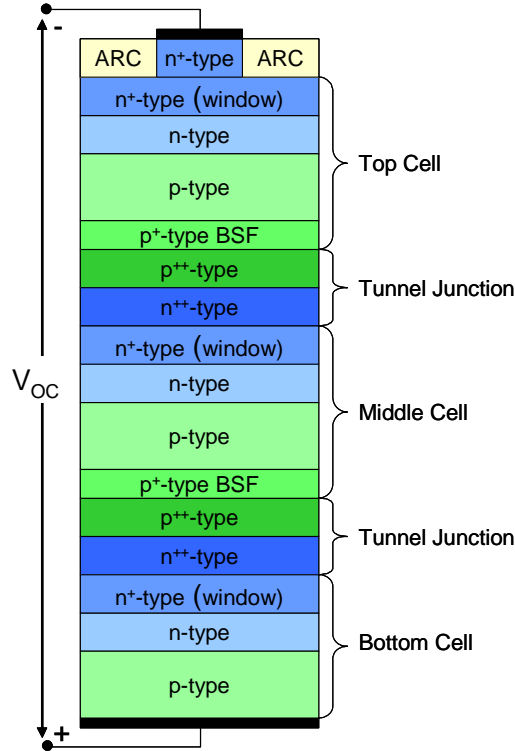
Figure 2.   Typical Layers of a Triple-Junction Solar Cell [From: 14].

Several improvements have been made over time with additional layers added to the cells to increase efficiency. The tunnel junctions are heavily doped layers that set up a tunneling field that allows for charge to flow more effectively between the layers. The Back Surface Field (BSF) creates a more heavily doped p-type region that in turn creates another electric field that will increase the movement of minority carriers toward the depletion region. Window layers have also been added to create a gradient that smoothes out the lattice mismatch between layers [15]. The window layer reduces surface recombination, while being thin enough to allow the photons to pass through to the next layer without being absorbed. Even with these improvements, the ability to optimize the respective band gaps of the various junctions is hampered by the requirement that each layer must be lattice matched to all other layers.

B.   LATTICE MISMATCH AND DISLOCATIONS

As mentioned in the introduction of the thesis, matching of lattice structures between two different semiconductor materials allows the incorporation of band gap variation in the material without introducing a change in the crystal structure [12]. Because solar cells are made of multiple binary and ternary alloys, each with its own crystal structure and lattice constant, the lattice spacing will be different between the crystals. When layers which have different lattice constants are grown epitaxially a lattice mismatch is created. The lattice mismatch causes defects referred to as line defects or dislocations.

There are two types of dislocations: the edge and screw types. Edge dislocations, illustrated in Figure 3, are defects where an extra half-plane of atoms are introduced mid-way through the crystal, distorting nearby planes of atoms. This distortion in bonding can occur periodically due to the stress associated with lattice mismatch.
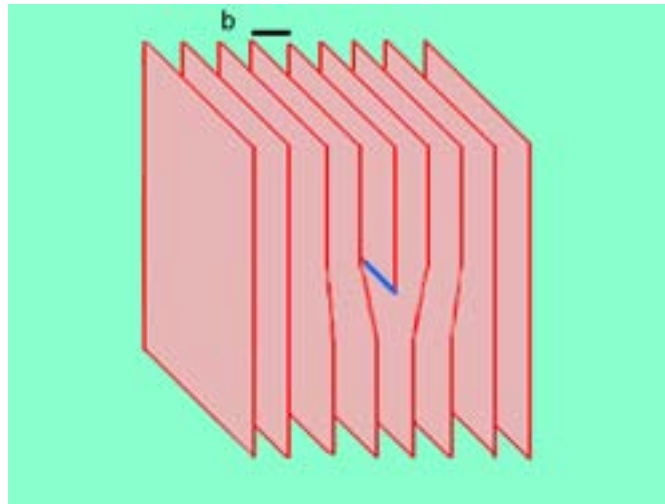
Figure 3.   Schematic Diagram Showing an Edge Dislocation [From: 16].

When enough force is applied from one side of the crystal structure, this extra plane passes through planes of atoms breaking and joining bonds with them until it reaches a grain boundary [16], [17], [18]. The screw dislocation may be considered as being produced by cutting the crystal partway through and pushing the upper part one lattice spacing over as shown in Figure 4.
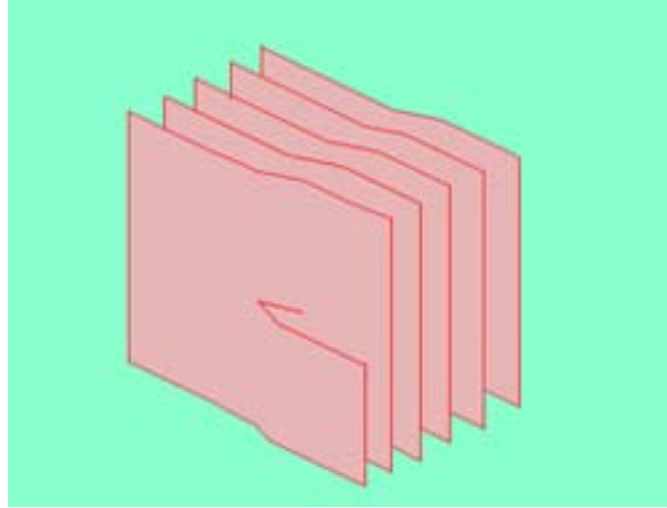
Figure 4.   Schematic Diagram Showing a Screw Dislocation [From: 16].

Line defects in devices are undesirable because they act as precipitation sites for metallic impurities and also serve as potential recombination sites which decrease the efficiency of charge collection and degrade device performance [9].

For heteroepitaxy, which is how triple junction solar cells are grown, the epitaxial layers and the substrate are three different semiconductors, and the epitaxial layers must be grown in such a way that an idealized interface must be continuous without interruption. Therefore, the adjacent semiconductors must either have the same lattice spacing or be able to deform to adopt a common spacing. These two cases are referred to as lattice-matched epitaxy and strained-layer epitaxy [9]. An example of lattice matched epitaxy is shown in Figure 5 where the substrate and the epitaxial layer have the same lattice constant. In the InGaP/GaAs/Ge triple junction solar cell, InGaP and Gallium Arsenide (GaAs) have a zinc blend crystal structure. Germanium (Ge) has a diamond crystal lattice structure. Table 1 shows the lattice constant of all three semiconductor materials and the percent variations between them.
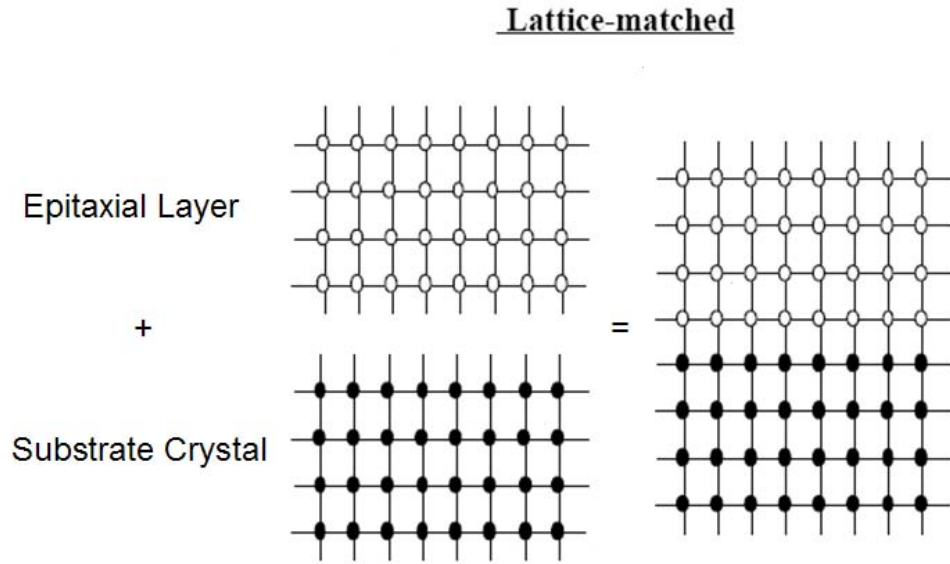
Figure 5.   Schematic illustration of a lattice-matched heteroepitaxial structure.

Material	Lattice Constant (Angstroms)	Percent Variation (%)
In$_{49}$Ga$_{51}$P	5.653	.0044
GaAs	5.65325	.084
Ge	5.658	-

Table 1.   Lattice constant and percent variation of semiconductor materials in the InGaP/GaAs/Ge Triple Junction Solar Cell.

The lattice constants are almost identical but still differ by approximately .0044 percent for InGaP and GaAs and approximately .084 percent for GaAs and Ge. Therefore, there are slight lattice-mismatches between the epitaxial layers, InGaP and GaAs, and the Ge substrate. Since the epitaxial layers have a lattice constant that is smaller than the lattice constant of the substrate, the epitaxial layer will be dilated in the plane of growth and compressed in a direction perpendicular to the interface.

In the strained-layer epitaxy, as the strained-layer thickness increases, the total number of atoms under strain or the distorted atomic bonds grows, and at some point misfit dislocations are nucleated to relieve the homogeneous strain energy. Figure 6 shows the case in which there are edge dislocations at the interface [9].

Lattice-mismatched
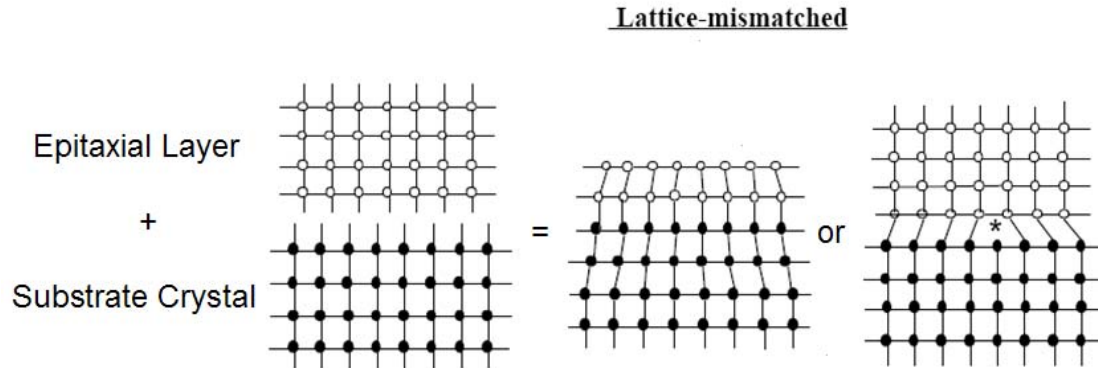
Figure 6.   Schematic illustration of a lattice-mismatched heteroepitaxial structure.

The inherent properties associated with the dislocations degrade the electrical and optical properties of the material. They can result in reduced mobility of minority charge carriers which will affect the diffusion length and lead to reduced power generation. The dislocations also affect the recombination luminescence by reducing the fraction of carriers that lead to band to band emission for a given generation rate. Figure 7 shows an image of light emission from an area of the InGaP material scanned with an electron beam.
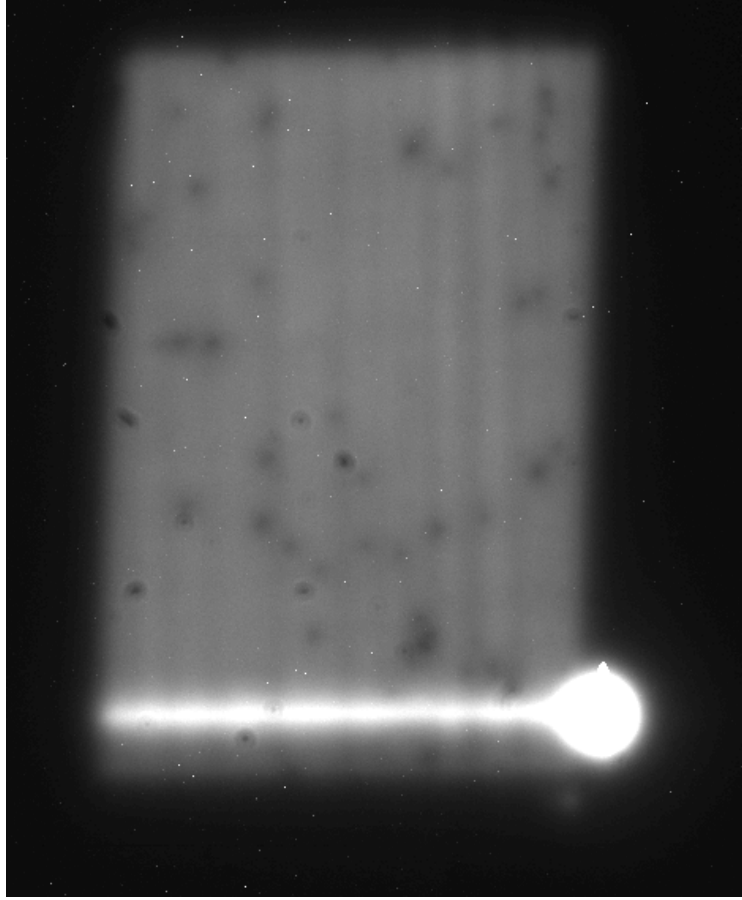
Figure 7.   Image of InGaP Luminescence Showing Light/Dark Dislocation Lines (400 μm x 337 μm).

The vertical dark bands in the image are caused by the dislocation pattern. There are various mechanisms that maybe responsible for the decrease in intensity within these dark bands. However, the accepted theory is that the dislocations reduce the minority carrier lifetime [19], [20], [21]. Since lifetime affects the diffusion length $\left(L_{diff} = \sqrt{\dfrac{\mu k T \tau}{e}} \right)$ one should predict a corresponding periodic variation of minority carrier diffusion length.

16

C.   TRANSPORT MODELING AND ASSUMPTIONS

Transport imaging utilizes the combination of a SEM for high resolution charge generation and a Silicon CCD in conjunction with an optical microscope (OM) for the recording of the spatially resolved luminescence. Upon exposure to the electron beam, a steady state spatial distribution of luminescence associated with charge recombination is created which can then be recorded by the CCD camera. The CCD images can be analyzed in order to provide quantitative measurements of local minority carrier diffusion. To extract the minority carrier diffusion lengths, there are a few assumptions that must be made. It has been experimentally established that the SEM beam's intensity follows a Gaussian distribution to first order [14]. In previous experiments it has been determined that the low injection limit, which means the minority carriers are recombining into a much larger and effectively constant number of majority carriers, is at $1x10^{-9}$ Amps of 30 keV electron beam current for studies of InGaP. Since the low injection limit of the material is dependent on doping, it is important to ensure that this assumption is still valid for this material.

The number of holes and electrons per unit volume for this sample of p-type InGaP is $= 1.10x10^{17} \text{cm}^{-3}$ and $= 2.11 \cdot 10^{-11} \text{cm}^{-3}$ respectively [14], [22], [23]. Δp and Δn would then be the number of holes and electrons per unit volume generated in steady state by the electron beam incident on the material. In order for the low injection limit to hold true for the modeling, $\Delta p << p$ and $\Delta n >> n$. The maximum electron-hole pair generation rate, neglecting electron beam energy loss due to backscattering can be calculated by $G = E_b \big/ E_i$, where E_b is the incident beam energy and E_i is the ionization energy of the electron-hole pair in InGaP. For electron beam energies in the 5-35 keV working range of the SEM, E_i is independent of incident electron beam energy and has been empirically determined to be $2.8E_g$ [24], where E_g is the bandgap of this InGaP sample, $\approx 1.81 \text{ eV}$ at 300 K.

The total minority population is then $\dfrac{I}{e}G\tau$ where I is the probe current and τ is the minority carrier lifetime in the InGaP heterostructure, ≈ 13.1 ns [14].

The minority carrier concentration in the generation region can then be calculated by using a hemispherical generation volume approximation for a 20 keV, 0.6 nA electron beam, following the development of Kanaya and Okayama [25]. This yields a minority carrier concentration of $\approx 2.70 \square 10^{17}$ cm^{-3}. Although $\Delta p \sim p$ the low injection limit model is still believed to be experimentally valid and therefore all of the experimental work will be done below the low injection limit.

In addition to the low injection limit model there are two other known ideas that are used in this work. The diffusion length of the InGaP/GaAs/Ge material is of sufficient magnitude that it does not approach the optical imaging system's resolution of ≈ 0.4 μm [26]. Finally is the assumption that the experimental results can be modeled as one dimensional, steady state diffusion due to the characteristics of the electron beam line scan, which will be discussed in more detail in the next section.

D.   1-D STEADY STATE MATHEMATICAL MODEL DEVELOPEMENT

1.   The Non-homogeneous Second Order Differential Equation Simplified

In this section the model for diffusion from a one dimensional source will be developed. An electron beam will generate a charge along a line and diffusion will be observed in one dimension from that line. The details of the experimental setup will be discussed in Chapter III. The one dimensional model allows the continuity equation to be greatly simplified and the minority carrier diffusion length easily extracted. The one dimensional steady state equation for the extraction of minority carrier diffusion length is developed, starting with the continuity equation for electrons in a p-type material:

$$\frac{dn}{dt} = G_n - U_n + \frac{1}{q}\left(\nabla \square \overrightarrow{J_n}\right) \tag{1}$$

where $\dfrac{dn}{dt}$ is the time rate of change of electrons per unit volume per second. This is given in terms of the generation rate, $G_n \left[\dfrac{1}{cm^3 s} \right]$, and the recombination rate, $U_n = \dfrac{\Delta n}{\tau_n}$ for low injection. Δn is the number of excess minority carriers available for recombination and τ_n is the effective lifetime for the electrons, which are non-equilibrium. $\vec{J_n}$ is the current density vector and is defined by the equation:

$$\vec{J_n} = q\mu_n n\vec{E} + qD_n \vec{\nabla} n \left[\dfrac{C}{cm^2 s} \right] \tag{2}$$

where μ_n is the mobility of minority carriers (electrons) and $\vec{E}$ is the externally applied electric field. D_n is the diffusion coefficient and is related to the diffusion length the by the equation:

$$L_{diff} = \sqrt{\dfrac{\mu kT\tau}{e}} = \sqrt{D\tau} \tag{3}$$

Using these relationships and substituting them into the continuity equation we get

$$\dfrac{dn}{dt} = G_n - \dfrac{n}{\tau_{eff}} + \dfrac{1}{q}\left[\vec{\nabla}\square\left(q\mu_n n\vec{E} - q\dfrac{L^2}{\tau_{eff}}\vec{\nabla} n \right) \right] \tag{4}$$

For this analysis we are assuming one dimensional, steady state conditions therefore the time rate of change of the minority carrier distribution is zero and the electric field is constant in the x-direction so that $\vec{E} = qE\vec{x}$. Equation (4) then becomes

$$0 = G_n - \dfrac{n}{\tau_{eff}} + \mu_n E\dfrac{dn}{dx} - \dfrac{L^2}{\tau_{eff}}\dfrac{d^2 n}{dx^2} \tag{5}$$

19

Rearranging equation (5) and multiplying through by $\dfrac{\tau_{eff}}{L^2}$ we get

$$\frac{d^2n}{dx^2} + \frac{\mu_n E \tau_{eff}}{L^2} \frac{dn}{dx} - \frac{n}{L^2} = -G_n \frac{\tau_{eff}}{L^2} \qquad (6)$$

and since there is no electric field applied $E = 0$. So now equation (6) can be simplified to

$$\frac{d^2n}{dx^2} - \frac{n}{L^2} = -G_n \frac{\tau_{eff}}{L^2} \qquad (7)$$

Equation (7) is a second-order non-homogeneous equation that can be easily solved for the minority carrier distribution. However, since we are assuming that due to the small thickness of the material there is no bulk photo-generation [10] the generation rate is zero away from the actual excitation source and thus Equation (7) can now be written as

$$\frac{d^2n}{dx^2} - \frac{n}{L^2} = 0 \qquad (8)$$

This is a second-order homogeneous equation whose general solution is

$$n(x) = Ae^{-x/L} + Be^{x/L} \qquad (9)$$

If we apply the boundary conditions at $x = 0, n(x) = n_{max}$ and at $x = \infty, n(x) = 0$ then Equation (9) becomes

$$n(x) = n_{max} e^{-x/L} \qquad (10)$$

Equation (10) represents the minority charge carrier distribution assuming one dimensional diffusion of the excess carriers.

2.   Charge Carriers Concentrations in Semiconductors

At a given temperature, thermal energy in a semiconductor results in the excitation of electrons from the valence band to the conduction band and leaves an equal number of holes in the valence band [9]. These bands are separated by a region of forbidden energy levels called the band-gap. Once the electron has gained enough energy

to move to the conduction band it is free to move within the band. The hole that is left behind by the excited electron is free to be filled by another electron in the valence band. Therefore, the holes are treated as positive charge carriers within the valence band and electrons are treated as negative charge carriers within the conduction band.

An undoped semiconductor at steady state and in thermal equilibrium will have the same number of positive charge carriers as negative charge carriers. The equation that governs this equilibrium condition is called the mass action law,

$$n_o p_o = n_i^2 \tag{11}$$

where n_o is the electron charge carrier concentration, p_o is the hole charge concentration, and n_i is the average intrinsic carrier concentration.

When a semiconductor is doped with impurities, they can be in the form of donor impurities or acceptor impurities. Donor impurities increase the number of free electrons, whereas, acceptor impurities lack a certain number of electrons needed to complete a bond thus creating a hole. N-type semiconductors are doped with donor impurities that contribute a number of electrons that are free to move in the conduction band. P-type semiconductors are doped with acceptor impurities that have excess holes in the valence band. In n-type and p-type semiconductors the concentration of dopant impurities is N_D or N_A respectively, which leads to the equations

$$n_i^2 = n_{po} p_{po} = n_{po} N_A \text{ (p-type material)} \tag{12a}$$

$$n_i^2 = n_{po} p_{po} = p_{po} N_D \text{ (n-type material)} \tag{12b}$$

where in Equation (12a) n_{po} and p_{po} are the electron concentration in p-type material (minority electron carrier concentration) and hole concentration in n-type material (minority hole carrier concentration) respectively.

Under external excitation, such as photons or an electron beam, additional electron-hole pairs are produced in the semiconductor, and Equations (11), (12a), and (12b) are no longer applicable [14]. In p-type semiconductors under low excitation

conditions $(\Delta p \ll p_o)$ the change in majority carrier concentration is small compared to the large change in minority carrier concentration $(\Delta n \gg n_o)$ when externally excited. Therefore, it is the behavior of the minority carrier concentration that is important in understanding semiconductor electrical and optical properties, under non-equilibrium conditions.

3. Diffusion, Mobility, and Lifetime

Diffusion in a semiconductor is the process of charge carriers moving from a region of high concentration to a region of low concentration. The diffusion coefficient or the diffusivity can be written as

$$D \equiv v_{th} * l \tag{13}$$

where v_{th} is the thermal velocity of the electrons and l is the mean free path. Using the theorem for the equipartition of energy for the one-dimensional case,

$$\frac{1}{2} m_n v_{th}^2 = \frac{1}{2} kT \,,$$

Equation (13) becomes

$$D = v_{th} * l = v_{th} \left(v_{th} * \tau \right) = v_{th}^2 \left(\frac{\mu_n * m_n}{q} \right) = \left(\frac{kT}{m_n} \right) \left(\frac{\mu_n * m_n}{q} \right)$$

$$D = \left(\frac{kT}{q} \right) * \mu_n \tag{14}$$

where k is the Boltzmann's constant, T is the temperature in Kelvin, and μ is the mobility. The diffusion coefficient is a function of mobility, which is a measure of the ease with which charge carriers move in the material [27]. The mobility will differ for electrons compared to holes because it is a function of their effective masses which also differ. The diffusion coefficient is also used to calculate one of the most important parameters of a semiconductor, the minority carrier diffusion length.

22

The diffusion length is the average length a charge carrier, electron or hole, diffuses before it recombines. The diffusion length $\left(L_{diff} \right)$ is given by the equation

$$L_{diff} = \sqrt{\frac{\mu k T \tau}{e}} = \sqrt{D\tau} \tag{15}$$

with all the variables previously defined from Equation (3). Equation (15) contains all the important parameters that determine a semiconductor's electrical properties such as; carrier diffusion length, mobility, and minority carrier lifetime.

In this work, cathodoluminescence was used to measure the luminescent intensity of the electron beam on the semiconductor sample. Then using the 1/slope technique developed and refined in [14] and described in Chapter 4, the diffusion length of the semiconductor sample is determined. The maximum luminescent intensity is then graphed and compared to the extracted minority carrier diffusion length to determine if any correlation between them exists.

4.   Luminescence in Semiconductors

One primary mechanism of luminescence in semiconductors involves the radiative recombination of electron-hole pairs [20]. An incident photon initially excites a valence band (VB) electron to the conduction band (CB). The electron then loses the excess energy as it interacts with the lattice, and falls close to the minimum CB energy. In one process, the electron can be captured into an excited state of a luminescent center or an activator. The electron then falls down in energy to the ground state of the activator and recombines with a hole in the VB releasing a photon, which is the luminescent emission. The photon released has energy that is approximately equal to the band gap energy of the material [10]. The electron-hole recombination is primarily radiative and is referred to as a radiative recombination process. It is this process of cathodoluminescence, shown in Figure 8 that is used to ultimately measure the diffusion length of the material in this work.
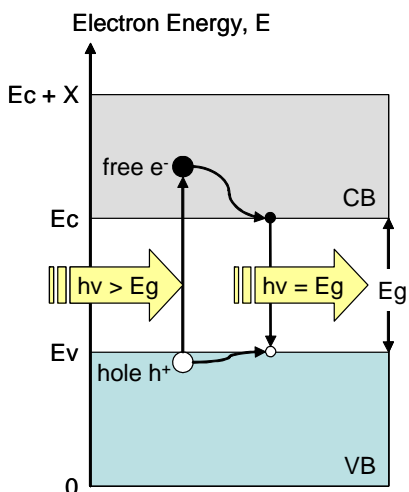
Figure 8.   Electron-Hole Creation via Photon Absorption and Recombination [From: 14].

While radiative recombination under e-beam excitation leads to cathodoluminescence, impurities and defects are known to introduce recombination processes that do not emit photons and are referred to as non-radiative recombination [20], [28], [29]. Non-radiative recombination is comprised of three main processes; Shockley-Read-Hall (SRH) recombination, Auger recombination, and surface recombination. The SRH recombination mechanism involves deep impurities or defects that are usually situated in the middle of the forbidden gap between the valence and conduction band [30]. These intermediate energy states or traps can temporarily capture an electron from the conduction band and localize it. Figure 9 shows the forbidden gap of a semiconductor that has an energy trap within it.

Figure 9.   Schematic Representation of the Trapping Mechanism [From: 32].

The time the electron spends trapped at the localized energy level, E_t, depends on the energy depth of the trap from the conduction band. After awhile, strong lattice vibrations due to thermal excitation will return the electron back into the conduction band. The time interval between photo-generation and recombination can be relatively long if the electron remains trapped at E_t for a considerable length of time or if the electron is captured multiple times before recombination [10]. In low injection, the majority-carrier density is much greater than the minority-carrier density. After minority-carrier capture, the center is reset by the subsequent capture of a majority carrier. Because of the relatively high concentration of majority carriers, capture occurs at a very high rate. Thus, in low injection, the SRH lifetime is determined solely by the minority-carrier capture rate. In high injection or with large cross-section ratios, this assumption cannot be made [21].

Auger recombination occurs when free energy obtained during recombination is transferred to an electron or a hole as kinetic energy which is subsequently dissipated by emission of multiple phonons until the charge carrier reaches the band edge [30]. Usually, Auger recombination is important when the carrier concentration is very high as a result of either high doping or high injection level [9].

Auger recombination effects are most frequently seen at high injection levels in Light Emitting Diodes (LEDs) and solid state lasers. The recombination rate varies with np^2 in p-type nondegenerate semiconductors. Thus, the Auger process is usually seen at relatively high carrier concentrations [21].

The final non-radiative recombination source that will be introduced is surface recombination. The surface of a semiconductor is an inherent source of various defects. Because of the abrupt discontinuity of the lattice structure at the surface, a large number of localized energy states or generation-recombination centers may be introduced at the surface region. These surface states greatly enhance the recombination rate at the surface region [9]. They are caused by dangling bonds at the crystal surface that result from the interruption of periodicity.

Also, the surface is a getter for impurities. These impurities range from atmospheric gases to metals. The surface impurities may also be a source of surface states and may coexist with dangling bond states [21].

Now that both radiative and non-radiative lifetimes have been explained it is time to show how they relate to the minority carrier lifetime. The recombination centers are characterized by a rate of recombination $R \propto \tau_r^{-1}$, where τ_r is a recombination time. When competitive radiative and non-radiative centers are both present, the observable lifetime is give by

$$\frac{1}{\tau} = \frac{1}{\tau_r} + \frac{1}{\tau_{nr}}$$
(16)

where τ_r and τ_{nr} are the radiative and non-radiative recombination lifetime, respectively. Also, τ_{nr}, in general, is the resultant of the multiple non-radiative recombination processes already introduced and can be denoted

$$\frac{1}{\tau_{nr}} = \sum_i \tau_{nri}^{-1}$$
(17)

Rearranging Equation (16) we get

$$\tau = \frac{\tau_r \tau_{nr}}{\tau_r + \tau_{nr}}$$ (18)

If we make the assumption that $\tau_r \gg \tau_{nr}$, as is often the case [20] then Equation (18) becomes

$$\tau = \tau_{nr}$$ (19)

which implies that the minority carrier lifetime is primarily dependent on the non-radiative lifetime. However, non-radiative lifetimes are dependent on material, doping, lattice matching, etc. The assumption that the radiative lifetime is much greater than the non-radiative lifetime causing the effective lifetime to be primarily dependent on the non-radiative lifetime is consistent with theory and work conducted in [9], [20], [21], and [28].

Lastly, the theoretical derivation of intensity distribution for recombination resulting from diffusion in one dimension is given. Previous work has shown the $I \square n$ relationship, where n is the minority carrier concentration, with respect to diffusion length as

$$Intensity \sim n \approx \frac{e^{-\frac{r}{L_{diff}}}}{r}$$ for the diffusion into three dimensions from a point source and

$$Intensity \sim n \approx K_o \left[\frac{r}{L_{diff}} \right]$$ for the diffusion into two dimensions. For this work from

Equation (10) the distribution, and hence the photon intensity from electron-hole recombination can be approximated as:

$$n \sim Intensity = I_{max} e^{-\frac{x}{L_{diff}}}$$ (20)

The boundary conditions $x = 0, I(x) = I_{max}$ and at $x = \infty, I(x) = 0$ are consistent with the observed results.

Now Equations (10), (19), and (20) can be used to show the relationship between the minority carrier concentration, the minority carrier lifetime, and the intensity. The relationship

$$n_{gen} = n_{max} = \frac{GI_b\tau}{e} \tag{21}$$

where all variables are as previously defined, is shown in [20] and represents the minority carrier population at the generation point. Equation (21) can be substituted into Equation (20):

$$n(x) = n_{max}e^{-\frac{x}{L_{diff}}} = \frac{GI_b\tau}{e}e^{-\frac{x}{L_{diff}}} \sim Intensity = \frac{GI_b\tau}{e\tau_r}e^{-\frac{x}{L_{diff}}}. \tag{22}$$

In the low-injection case, the intensity is proportional to the minority carrier concentration with the constant of proportionality equal to the inverse of the radiative lifetime, τ_r. Since the intensity is dependent on electron beam current there can be assumed a linear dependence of the intensity on the stationary excess carrier density. Therefore, the total intensity can be expressed as

$$I_{tot} = \int_V f\frac{\Delta n(r)}{\tau_r}d^3r \tag{23}$$

where f is a function containing correction parameters of the detection system and factors that account for the fact that not all photons generated in the material are emitted (due to optical absorption and reflection losses). This is the three dimensional equation and can be simplified to Equation (24) since we are only dealing with a one-dimensional analysis.

$$I_{tot} = \int f\frac{\Delta n(x)}{\tau_r}dx \tag{24}$$

In Equation (24) Δn is the excess carrier density $\Delta n = (n - n_o)$, τ_r and f are as previously defined [20]. The total intensity is just the total area beneath the intensity curve shown in Figure 10 and calculated by

$$I_{tot} = 2\int_0^\infty I_{max} e^{\frac{-x}{L_{diff}}} dx \qquad (25)$$
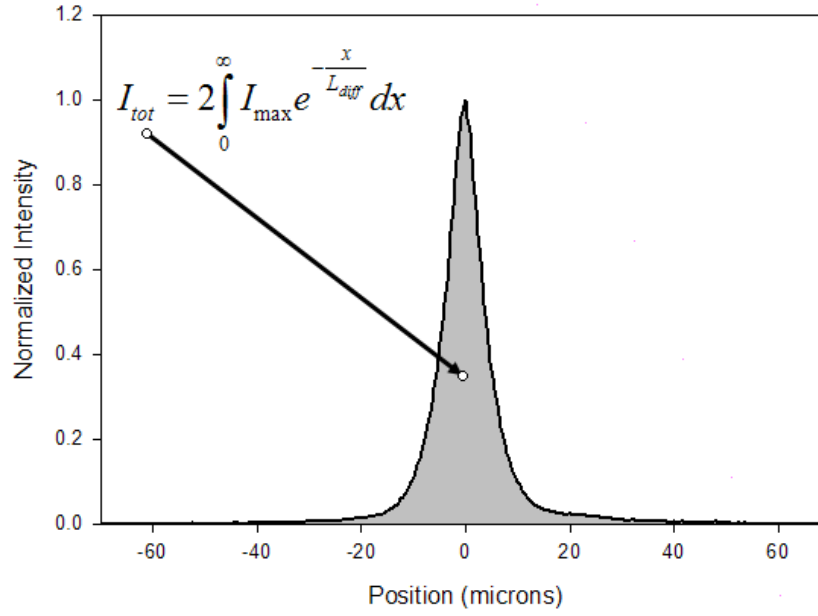
Figure 10.   A Normalized Intensity Curve Illustrating the Physical Definition of Total Intensity

Therefore,

$$I_{tot} = 2I_{max}L_{diff} \qquad (26)$$

Now Equations (24) and (26) can be related as follows

$$2I_{max}L_{diff} = I_{tot} = \int f \frac{\Delta n(x)}{\tau_r} dx \text{ and } \Delta n \text{ can be represented by } \Delta n = n - n_o$$

29

where $n = n_{max} e^{\frac{-x}{L_{diff}}}$ and $n_o = n_{max} e^{\frac{-x_o}{L_{diff}}}$ and since we can also assume that $n \gg n_o$ then $\Delta n = n$ so we get the equation

$$2 I_{max} L_{diff} = \frac{f * n_{max}}{\tau_r} \int_0^\infty e^{\frac{-x}{L_{diff}}} dx \qquad (27)$$

With the further assumption f is constant and taking the integral in Equation (27) the equality becomes

$$I_{max} = \frac{f}{2\tau_r} n_{max} \qquad (28)$$

where n_{max} is a constant, τ_r is as defined previously, and $f = f_D f_A f_R$. The constant factor f_D accounts for such parameters of the detection system as the overall collection efficiency of the light collector, the photomultiplier (or solid-state detector) quantum efficiency, the transmissive efficiency of the monochromater, and the signal amplification factor. The f_R constant factor accounts for the refraction and total internal reflection. The f_A constant factor or absorption loss factor arises from a decrease in intensity of the form $\exp(-\alpha d)$, where α is the absorption coefficient and d is the length of the photon path in the interior of the material [20]. Since we are working with a one dimensional analysis, f_A is not applicable and the other two constant factors only affect the magnitude of the intensity but not the behavior and will not be included in this analysis. Therefore, we now have the equation:

$$I_{max} \approx \frac{n_{max}}{2\tau_r} \qquad (29)$$

To get the relationship between τ and the intensity, the equation

$$n_{max} = g * \tau \qquad (30)$$

must be applied to Equation (29). In Equation (30), g is the minority carrier generation rate and the other variables are as previously defined.

When Equation (30) is substituted into Equation (29) we get

$$I_{\max} \approx \frac{g * \tau}{2\tau_r} \tag{31}$$

If we use the relationship for the lifetime derived in Equation (19) we obtain

$$I_{\max} \approx \frac{g * \tau_{nr}}{2\tau_r} \tag{32}$$

Equation (32) shows that if the radiative recombination lifetime gets shorter then the maximum intensity will increase, whereas, if the radiative recombination lifetime gets longer, the intensity will decrease for a fixed τ_{nr}. Using this idea and revisiting the assumptions that τ_r is constant and $\gg \tau_{nr}$ will be key ideas in analyzing the variations in intensity and diffusion length and comparing their correlation.

THIS PAGE INTENTIONALLY LEFT BLANK

III.   EXPERIMENTAL APPARATUS

A.   DIRECT DIFFUSION IMAGING

The direct diffusion imaging technique first presented in [27] and again in the Mill's thesis, [14], illustrates a way to experimentally obtain the diffusion length of minority carriers in semiconductor materials. The focus of this work is also on the p-type layers of a triple junction solar cell.   This technique directly images the radiative recombination of electron-hole pairs.   This process is similar to conventional cathodoluminescence (CL), where the external source for generating electron-hole pairs is an electron beam. The electron beam is held over a fixed position on the sample and the production and radiative recombination process of electron-hole pairs are at steady-state. In standard CL, much of the light does originate at or very near the point of charge generation, however, any distribution of the luminescence, whether due to drift, diffusion or interaction volume is lost.   In transport imaging, the spatial information of the electron-hole pair recombination is retained, therefore, the transport of minority charge can be observed. This method can be applied without any additional sample preparation or need for electrical contacts on the sample [14].

B.   EQUIPMENT

The system consists of a JEOL 840A SEM with an internal optical microscope. A modified, liquid helium-cooled SEM stage from Oxford Instruments allows for the sample to be studied at temperatures from 5 – 300K [14]. Variable temperature will not be used for the purposes of this thesis, but is mentioned for completeness. Figure 11 shows the SEM with the modified stage and the optical microscope attached.

Figure 11.   JEOL 840A SEM with Modified Stage and Optical Microscope [From: 14].

The optical detector is a thermoelectrically-cooled Apogee silicon charge coupled device (CCD) camera with a 2184 x 1472 pixel array. During normal operation, the CCD camera is normally cooled to approximately $-20°$ C to reduce the noise and collects unfiltered light from 400 to 1100 nm wavelengths. The pixel size of the camera is 8.6 x 8.6 μm and the resolution of the resulting image is approximately 0.4 $\mu m/\text{pixel}$. This resolution is close to the diffraction limit for the observation of luminescence from room temperature GaAs at 870 nm. Figure 12 shows the CCD camera and Figure 13 shows a schematic of the full system with the modified stage.

Figure 12.   Apogee 2184 x 1472 Cooled CCD [From: 14].
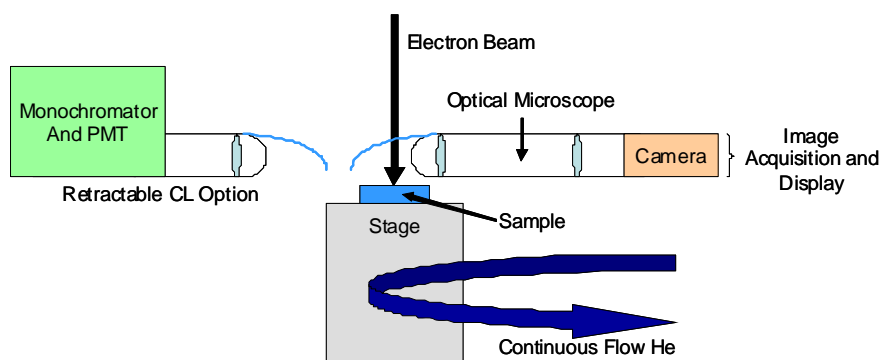
Figure 13.   Schematic of Transport Imaging Components [From: 14].

The SEM operating modes used in this work are the picture mode, line mode, and spot mode. These modes refer to the rastering of the electron beam in an area (picture), in a line (line), or a fixed (spot). The picture mode is primarily used to ensure that the dark and light dislocation bands are perpendicular to the line scan since we are only interested in the variation of the diffusion length within the bands themselves. This mode was used in conjunction with the spot mode to get a good focus of the sample area and to choose a sample area to be scanned that had minimal surface defects.

In picture mode, the SEM electron beam is rastered in x and y and the luminescence is imaged by the CCD. Figure 14 shows an image taken in SEM picture mode of doped p-type $In_{.49}Ga_{.51}P$. $In_{.49}Ga_{.51}P$ is comprised of 49 percent indium and 51 percent gallium. A detailed description of this material's growth process and characteristics are presented in Chapter IV.
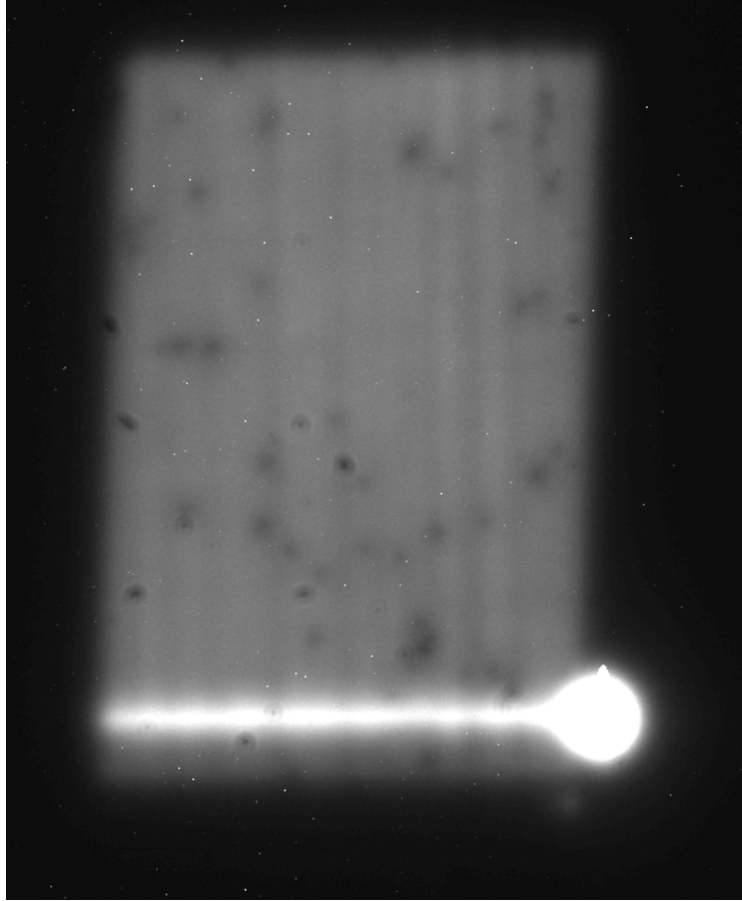
Figure 14.   Image of InGaP in Picture Mode at a Probe Current of $6x10^{-10}$ A and electron beam energy of 20 keV (400 μm x 337 μm).

The bright edge with the large luminescence spot in the bottom right corner results from the SEM scanning one edge of the raster area longer than the rest of the area. For synchronization of the scan, Figure 15 shows a combined image of the picture mode with the line scan mode that was used to ensure a perpendicular line scan.

Figure 15.   Image of InGaP in Combined Picture and Line Scan Modes with the Electron Beam Rotated to Scan Horizontally (400 μm x 337 μm).

In a majority of the work accomplished for diffusion length imaging, the spot mode is the primary mode of operation. In the spot mode the electron beam is held fixed on the sample and the distribution of the resultant luminescence in two dimensions show the diffusion of the minority charge carriers [14]. Figure 16 shows a spot mode image taken on the sample of $In_{.49}Ga_{.51}P$. It is important to note that the bright, observable spot that is seen is much greater, in this material, than the diameter of the incident electron beam.
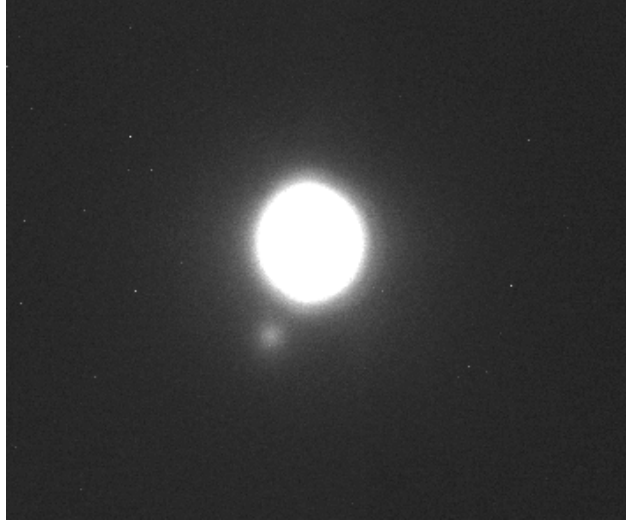
Figure 16.   Image of InGaP in Spot Mode with the Optical Reflection in the Lower Left at a Probe Current of $6x10^{-10}$ A and electron beam energy of 20 keV (400 μm x 337 μm).

The spot image is the actual sample luminescence created by the electron-hole recombination as the electrons diffuse away from the generation source. So the region of interaction is what is analyzed in order to gather information about the minority charge carrier properties. In this thesis the spot mode was mainly used in conjunction with the picture mode to ensure focus, to extract sample data for diffusion length calculation, and to determine the effects on the diffusion length caused by the small optical reflection spot that is seen just to the bottom left of the primary electron beam spot shown in Figure 16. The results of this analysis will be discussed in the next chapter of this thesis.

The primary mode of operation for this work was the line scan mode. Figure 17 shows an example of a horizontal line scan on the InGaP sample. The line scan generates a one dimensional line across the surface of the thin sample simulating a long thin wire. This allows a one dimensional analysis to be conducted as the minority carrier population has net diffusion in one direction away from the point of generation. The line scan mode can be used to make a horizontal line scan or a vertical line scan by adjusting the beam rotation angle on the SEM control panel.

The line scan mode with a horizontal rotation imaged across the dislocation bands was seen in Figure 15, where as the line scan mode with a vertical rotation imaged within the dislocation bands is shown in Figure 18. The next chapter explains the modeling and analysis technique used to extract the diffusion length and maximum intensities from the line scan image.
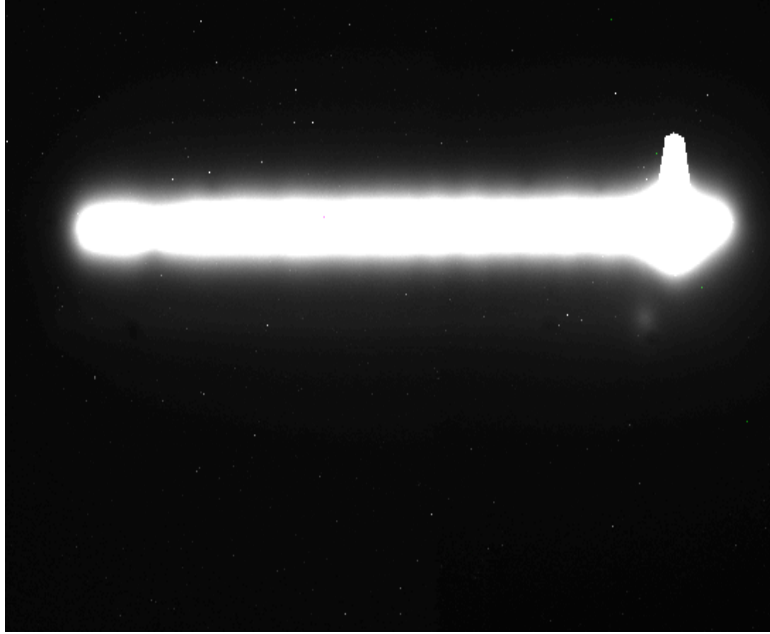
Figure 17.   Image of InGaP in Line Scan Mode Rotated Horizontally at a Probe Current of $6x10^{-10}$ A and electron beam energy of 20 keV (400 μm x 337 μm).
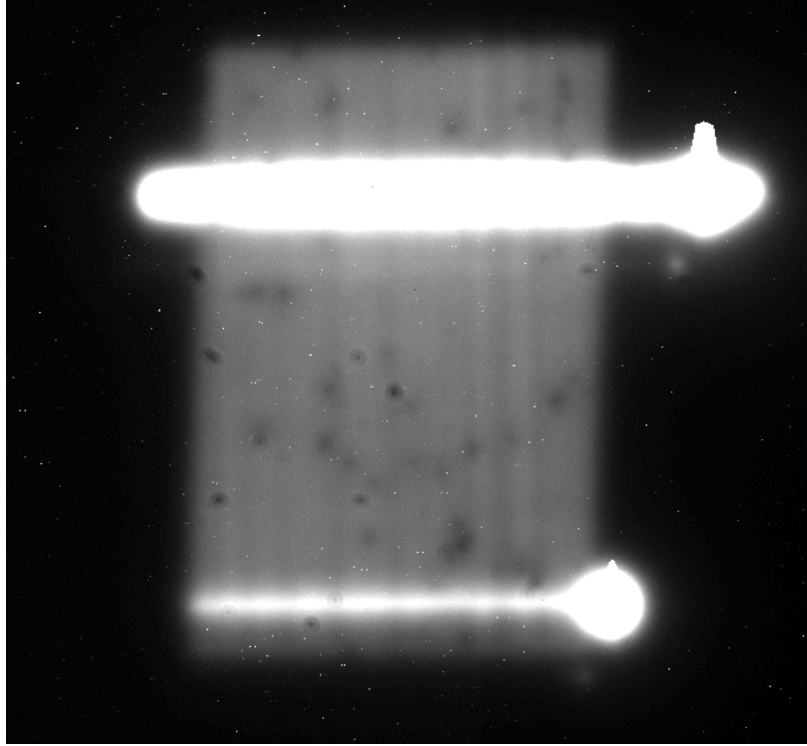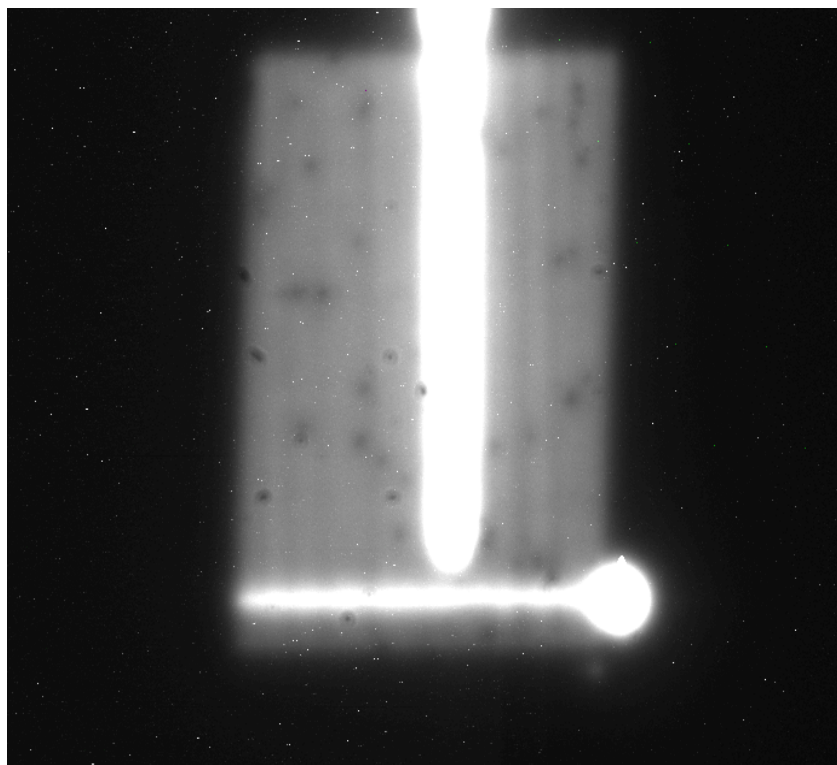
Figure 18.   Image of InGaP in Combined Picture and Line Scan Modes with the Electron Beam Rotated to Scan Vertically (400 μm x 337 μm).

IV. DIFFUSION LENGTH AND INTENSITY VARIATION CORRELATION STUDY

A. TRIPLE JUNCTION SOLAR CELL MATERIAL DESCRIPTION

Using the approach that will be described in the next section, the spatial variations in diffusion length and luminescent intensity will now be measured and an analysis of the results will be presented. The sample is a double heterostructure of the top junction p-type layer within the triple junction solar cell and is composed of AlGaInP/InGaP/AlGaInP grown via metalorganic chemical vapor deposition (MOCVD) on (001) Ge substrates.

The double heterostructure configuration and the band diagram of the sample is illustrated in Figure 19.
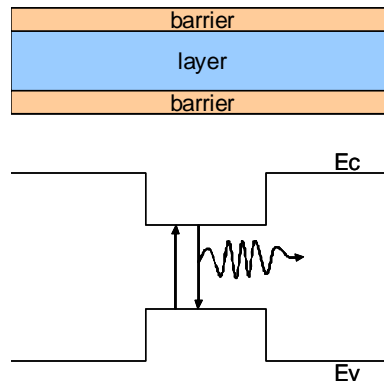
Figure 19. General Schematic of a Double Heterostructure and the Band Diagram [From: 14].

The double heterostructure is important for transport imaging for two reasons. The thin double heterostructure can be treated as a two dimensional structure, which can be further simplified to a one dimensional structure using the line scan mode mentioned in Chapter three. Also, surface recombination of the minority charge carriers is eliminated by the two barrier layers. By removing the potential influence of surface recombination, the measured diffusion lengths are more fundamentally representative of the layer material [14].

The In$_{.49}$Ga$_{.51}$P layer is the top cell in this triple junction solar cell sample. The layer thickness of In$_{.49}$Ga$_{.51}$P for this sample is on the order of ~.7 μm. This particular alloy of InGaP has a band-gap of 1.81 eV which is the largest band-gap of all the cells and therefore absorbs the higher energy photons compared to the rest of the cell. Table 2 shows the band-gap for some of the various types of semiconductor materials used in solar cells.

Material	Band-gap Energy (eV)
In$_{49}$Ga$_{51}$P	1.81
GaAs	1.42
Si	1.12
Ge	.661

Table 2.   Energy Band-gap of Various Semiconductor Materials.

The InGaP layer is arguably the most important layer in the triple junction solar cell. As shown in Figure 2 the triple junction solar cell has three cell layers stacked in series. In a series solar cell, the limiting cell is the one that produces the least amount of current. The I-V (current vs. voltage) characteristic curves for Ge, Si, GaAs, and InGaP solar cells under AM0 solar illumination are shown in Figure 20.
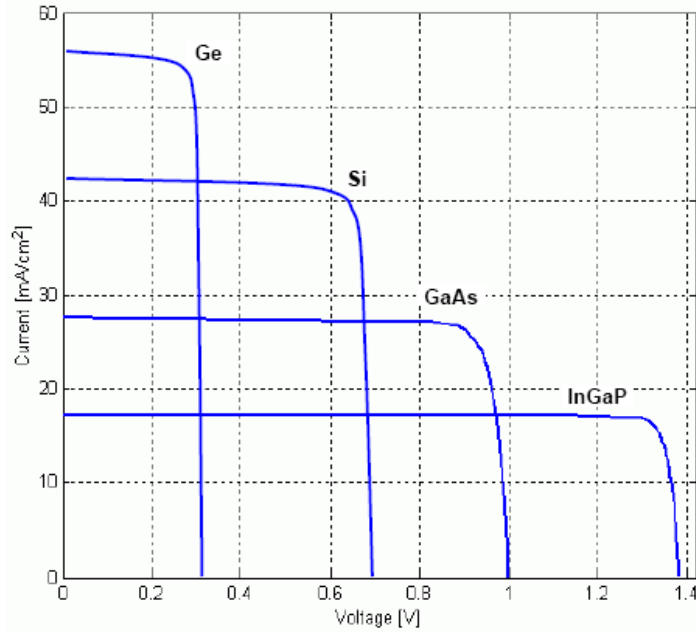
Figure 20.   I-V Curve for Ge, Si, GaAs, and InGaP Cells Under AM0 Solar Illumination [From: 14].

InGaP clearly produces the largest open circuit voltage; however, it also has the lowest short circuit current. Therefore, in triple junction solar cells, the InGaP layer is the limiting layer in regard to current flow throughout the cell [14].

Another characteristic of InGaP epitaxial material involves the ordering or disordering of the indium and gallium atoms. As mentioned briefly in Chapter three, $In_{.49}Ga_{.51}P$ is the alloy of InGaP that is lattice matched to Ge. The ordering of InGaP is due to the atomic arrangement of the Group III elements (In and Ga) on the Group III sub-lattice [14]. Figure 21 illustrates this arrangement by showing the zinc blende (ZnS) cubic crystal structure, which is the crystal structure of InGaP.
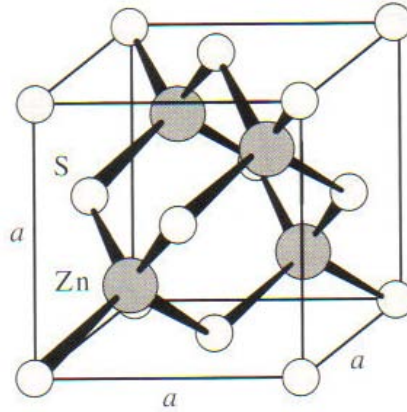
Figure 21.   Zinc Blende Cubic Crystal Structure [From: 14].

The atoms labeled S are the Ga/In atoms and the atoms labeled Zn are the P atoms. The ordering of the Ga/In plane within the crystalline structure is characterized by CuPt ordering, one of the most widely studied types of long range ordering with alternating planes occupied by atoms from the Group III elements. Figure 22 shows a simulation of the ordering and disordering of Group III or V sub-lattice for electron diffraction patterns done by Dobročka, Vávra , and Wallenberg that shows ordered and disordered domains of the CuPt-type ordering in the Ga/In plane [14].
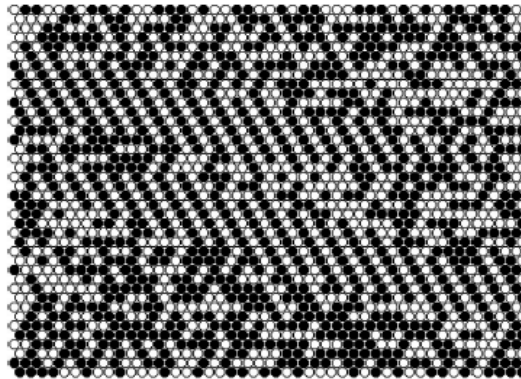
Figure 22.   Ordered and Disordered Domains of CuPt Ordering in III-V Semiconductor Alloys [From: 14].

The importance of the ordering in the Ga/In planes of InGaP is that the band-gap of InGaP is dependent on the ordering. The ordering allows for additional tuning of the band-gap within the InGaP layer of the triple-juction solar cell.

44

Higher efficiencies of output power can be obtained with a larger band-gap, since the tuning of the band-gap increases the open circuit voltage while not changing the short circuit current [14]. The $In_{.49}Ga_{.51}P$ sample used for this work was a lattice matched, ordered alloy.

B.   DIFFUSION LENGTH DATA EXTRACTION

1.   Slope Analysis Estimation

As illustrated in Equation (20), the diffusion length of minority charge carriers in a sample, excited externally at a point source, can be extracted by calculating the slope of a semi-logarithmic plot of intensity versus position. The slope would be represented on this semilog plot as

$$m = \frac{-1}{L_{diff}}$$
(33)

where m is the slope and L_{diff} is as previously defined. The sample used in this work was a p-type $In_{.49}Ga_{.51}P$ sample doped at a level of $1.10x10^{17}$ cm^{-3} and is used to illustrate the 1/slope technique of extracting diffusion length. The effective minority carrier lifetime of the double heterostructure, $In_{.49}Ga_{.51}P$, taken from [14] and determined from time-resolved photoluminescence is 13.1 nanoseconds. In Figure 17 an image of the diffusion of the minority charge carriers using the line scan excitation mode from the SEM at a probe current of $6x10^{-10}$ A and electron beam energy of 20 keV, for an exposure time of 3 seconds was shown.

From the image, a vertical line profile is taken and imported into SigmaPlot, the graphing and data analysis software used in this work. The data are then normalized and the noise floor of the CCD camera is subtracted via the equation:

$$I_{Norm} = \frac{I - I_{Noise}}{I_{Max} - I_{Noise}} \tag{34}$$

Figure 23 shows a plot of the normalized intensity as a function of position. A semi-logarithmic plot of the data is shown in Figure 24.
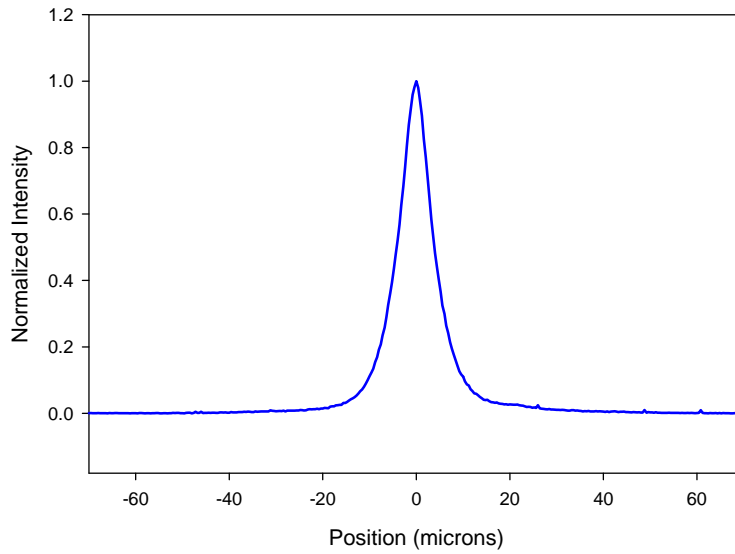
Figure 23.   Normalized Intensity as a Function of Position.
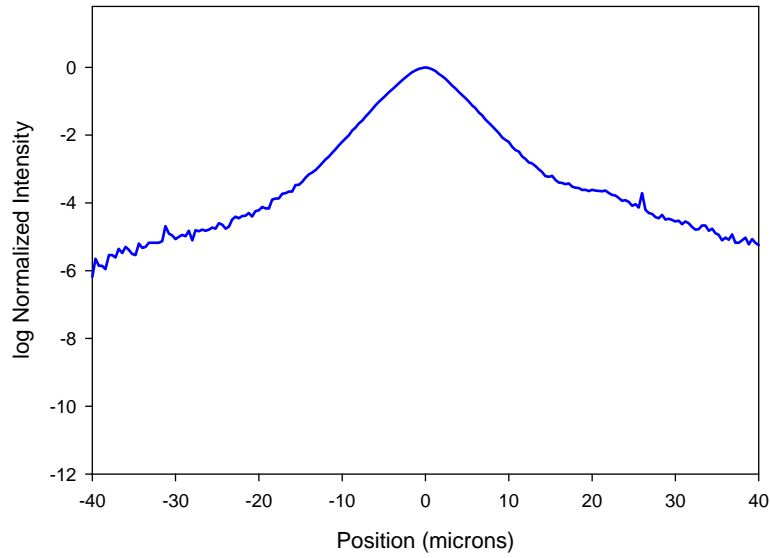
Figure 24.　　Semi-log Plot of the Normalized Intensity as a Function of Position.

The semi-logarithmic plot of the normalized intensity versus the position from the center of the charge generation as shown in Figure 24 is used to choose how far away from the charge generation center to evaluate the slope value. The errors in the slope value become smaller as the distance from the line center increases; however, the farther away from the line center, the more noise that distorts the data [14]. For this sample the slope value was extracted between 2 and 15.2 microns from the charge generation center. Figure 25 shows the data from the left and right sides of the normalized distribution and the linear regression lines extracted from the data.
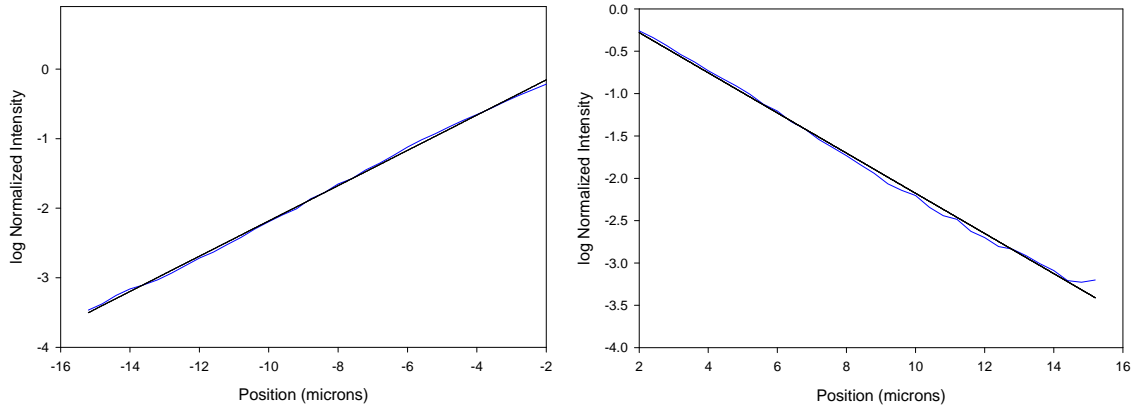
Figure 25.   Semi-log Plot of Normalized Intensity as a Function of Position and the Linear Regression Lines Used in Slope Extraction.

SigmaPlot contains a subroutine that was used to extract the slope value, the standard error, and the R^2 from the linear regression lines shown in Figure 25. The slope value is used to estimate the diffusion length, and the R^2 value is used to determine how well the data fit the linear regression. Table 3 shows the results of the linear regression and the estimated diffusion lengths extracted for the luminescence profiles to the right and left of the charge generation point [14].

SAMPLE	*SLOPE*	*StdErr*	$L_{diff}\ (1/slope)$	R^2
	μm^{-1}	μm^{-1}	μm	
InGaP/Ge (R)	-.237	.0025	4.22	.997
InGaP/Ge (L)	.254	.0014	3.94	.999

Table 3.   Linear Regression and the Estimated Diffusion Lengths Results Extracted for the Luminescence Profiles to the Right and the Left of the Charge Generation Point.

2. Eliminating the Diffusion Length Associated with the Optical Reflection

As shown in Figure 25 there are two sides to the normalized intensity distribution. This is due to the fact that the electrons diffuse out in opposing directions from the generation line. In Figure 16 an image was shown that was taken in the SEM's spot mode. To the lower left of the primary electron beam spot there is a small secondary spot that is the result of the secondary reflection of the main spot and the collecting optics in the optical system. This secondary reflection is also present in the line scan mode located in the same relative position as in the spot image and illustrated in Figure 26.
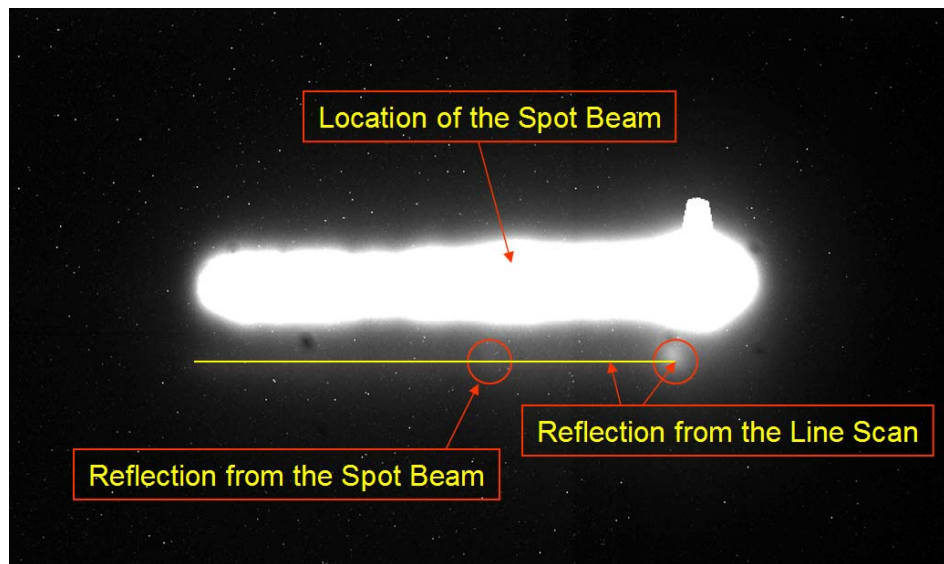
Figure 26.   Location of the Secondary Reflection in the Spot Beam Relative to the
Secondary Reflection in the Line Scan.

Created using MicroCCD, an imaging software tool, Figure 26 is a combined image of the spot beam image and the horizontal line scan image. The secondary reflection from the spot image can be seen to be inline with the secondary reflection from the line scan image. Using MicroCCD, data are extracted from the horizontal line scan image using a vertical line profile shown in Figure 27.
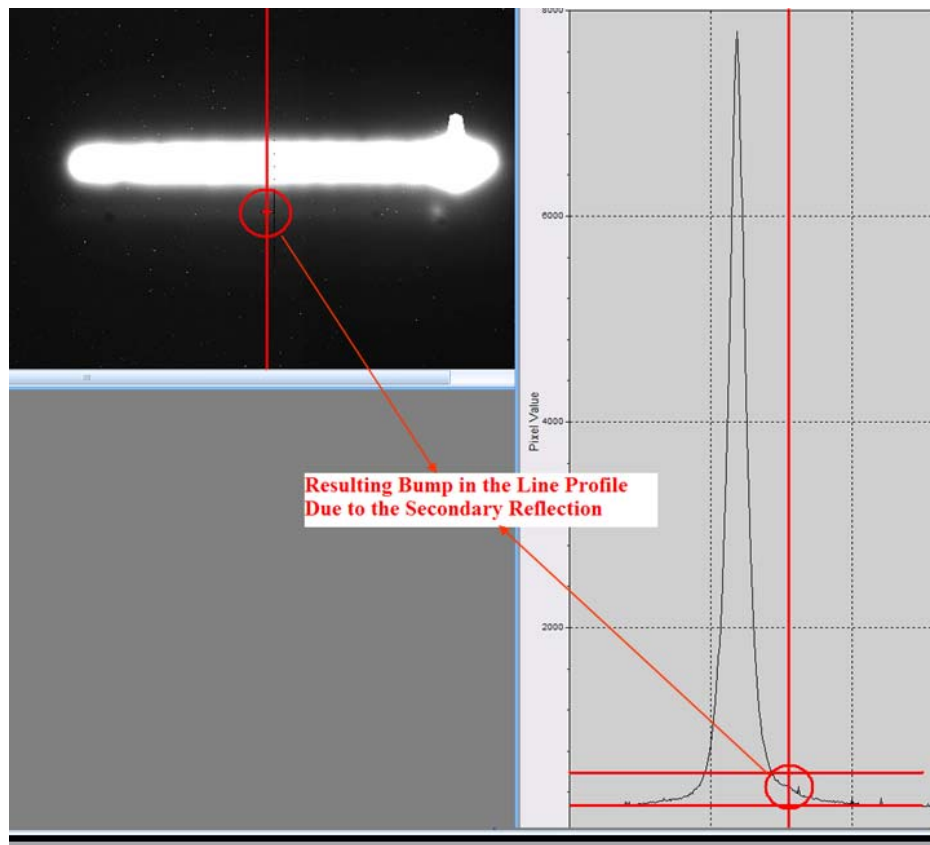
Figure 27.   Vertical Line Profile Taken Through the Secondary Reflection.

Figure 28 shows the actual and normalized intensity profiles of the horizontal line scan beam with a small bump in the curve where the reflection spot is located.
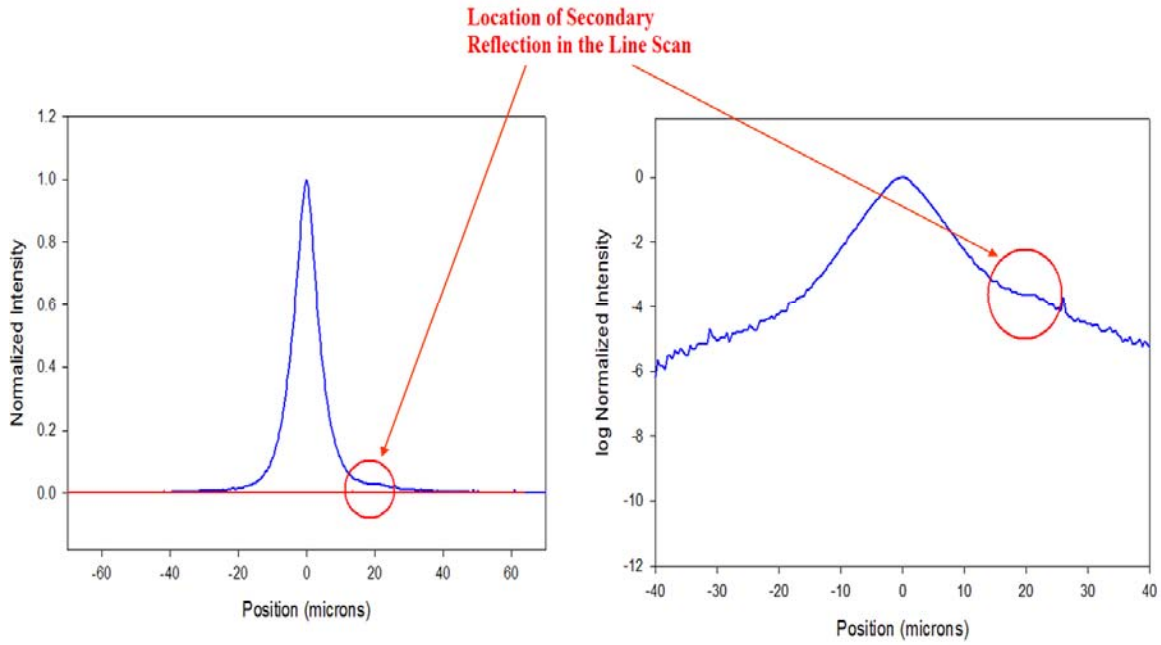
Figure 28.   Location of the Reflection Spot in the Normalized Intensity and Semi-log Normalized Intensity Profile Curves.

A linear regression analysis is then applied to find the diffusion length. Table 4 lists the diffusion lengths for several vertical line profiles for the left and right sides of the normalized intensity distribution and the value of the diffusion length determined for a vertical line profile in [14] in the $In_{.49}Ga_{.51}P$ sample at this doping concentration and with this specific scan rotation. Figure 29 illustrates the left and right side diffusion lengths extracted over a 60 micron portion of the horizontal line scan in which very few imperfections were visible in the sample.

L_{diff} $(1/slope)$ **Right Side**	L_{diff} $(1/slope)$ **Left Side**	*Ave* L_{diff} $(1/slope)$ *From Ref. 5*
μm	μm	μm
4.18	3.94	3.9
4.17	3.94	
4.18	3.92	
4.17	3.93	
4.15	3.90	
4.14	3.92	
4.17	3.91	
4.14	3.97	
4.16	3.94	
4.17	3.93	
4.18	3.94	
4.18	3.90	
4.16	3.88	
4.18	3.94	
4.17	3.91	
4.18	3.94	
4.19	3.91	
4.20	3.92	
4.18	3.93	
4.20	3.93	

Table 4.   The Left and Right Side Diffusion Lengths Over Several Vertical Line Profiles and the Previously Measured Diffusion Length from [From: 14].
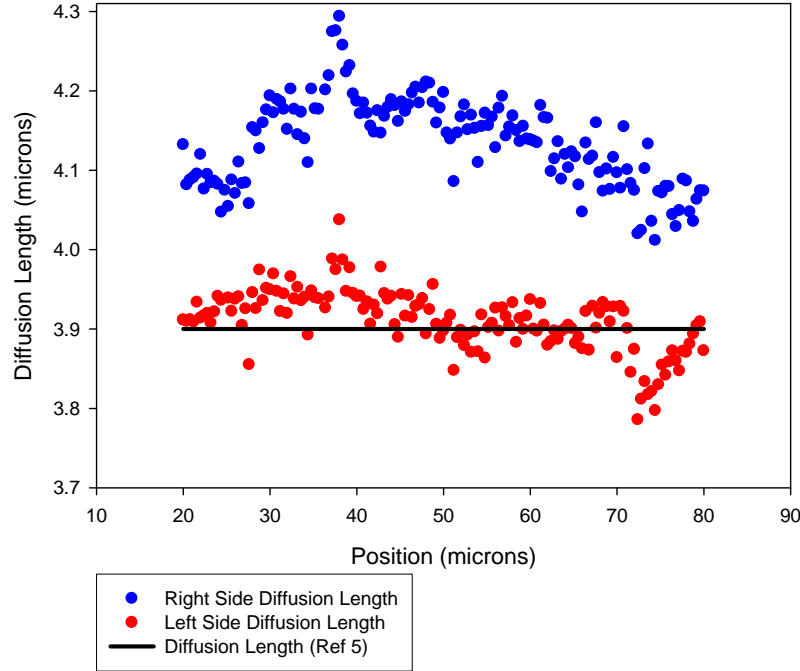
Figure 29.   Left and Right Side Diffusion Lengths Extracted Over a 60 Micron Portion of the Horizontal Line Scan.

It is important to compare the left and right side diffusion lengths and realize that in every case the side with the small bump due to the secondary reflection resulted in a diffusion length that was $\sim 4-7$ percent larger. It is apparent from the extracted data that the secondary reflection causes additional luminescence in that area of diffusion as we move away from the generation point source. That results in the artificially higher diffusion length on the right side of the intensity distribution. Since the secondary reflection is not a generation point source, but is a result of the optics of the system then its contribution to the luminescence intensity can be deemed invalid and the data for the right side of the normalized intensity distribution curve should be discarded.

In the case of the vertical line scan, the line scan is rotated 90 degrees; however the position of the optical system remains the same. This means that the position of the secondary reflection does not rotate and remains to the lower left of the spot beam. Therefore, the secondary reflection is on the left side of the vertical line scan. This

53

corresponds to the left side of the normalized intensity distribution curve. However; the secondary reflection is only slightly to the left of the maximum luminescent intensity, therefore, the vertical line scan for the most part overlaps the secondary reflection. This can be demonstrated by combining the spot image and the vertical line scan image in MicroCCD. Figure 30 shows the combined image of the electron beam spot and the vertical line scan.
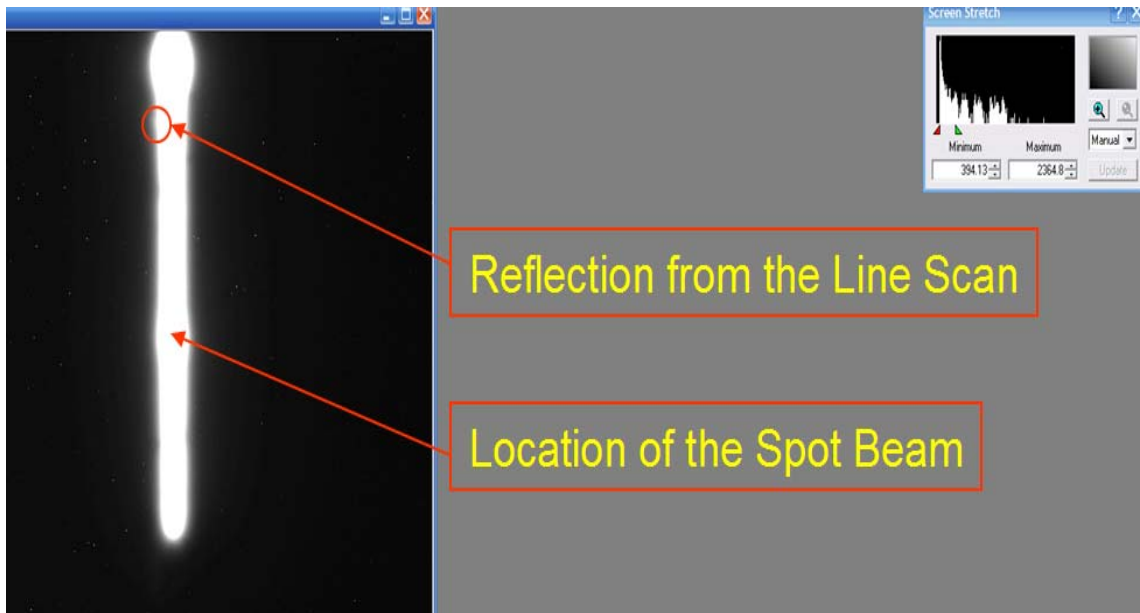
Figure 30.   Combined Image of the Electron Beam Spot and Vertical Line Scan.

For a vertical line scan the luminescence and position data are extracted via a horizontal line profile in MicroCCD. The linear regression analysis is applied as before and the diffusion length results are listed in Table 5.

L_{diff} $(1/slope)$ **Right Side**	L_{diff} $(1/slope)$ **Left Side**	*Ave* L_{diff} $(1/slope)$ *From Ref. 5*
μm	μm	μm
3.51	3.51	3.55
3.51	3.51	
3.53	3.51	
3.53	3.51	
3.50	3.52	
3.52	3.51	
3.49	3.51	
3.50	3.50	
3.49	3.53	
3.50	3.50	
3.48	3.49	
3.49	3.49	
3.47	3.50	
3.52	3.50	
3.51	3.52	
3.51	3.53	
3.51	3.52	
3.52	3.53	
3.50	3.57	
3.53	3.51	

Table 5.   The Left and Right Side Diffusion Lengths Over Several Horizontal Line Profiles and the Previously Measured Diffusion Length from [From: 14].

The average diffusion lengths for the vertical line scan are less than that for the horizontal line scan possibly due to crystallographic variations of scattering, thereby showing a dependence upon the direction within the semiconductor [14]. In addition, the secondary reflection is not predominately on the left side of the intensity distribution as it is in the horizontal line scan. So the diffusion lengths extracted from the left and right sides are comparable and differ by only less than a half of a percent with the left side diffusion length being closer to the known average value of the diffusion length in this orientation. So even though the secondary reflection is slightly on the left side of the normalized

intensity distribution curve, it does not have an appreciable effect on the differences in diffusion length. Therefore, since the diffusion length on the left side is actually closer to the known average value of the diffusion length in this orientation, then the data for the right side can still be discarded for the purposes of this analysis.

C. EXPERIMENTAL RESULTS

1. Initial Observations of Spatial Variations of Diffusion Length and Intensity

Although there has been a lot of investigations into dislocations in semiconductors and their correlation to luminescent intensity and minority carrier lifetime, there has been little data collected on diffusion length and how it varies with respect to dislocations in the crystal lattice structure. The initial goal of the measurements were to determine if the spatial variations that appear as the light and dark bands could be correlated to measureable variations in minority carrier diffusion length. Figure 31 shows the picture mode of the general location on the sample that these horizontal line scan images were taken and then illustrates where within that area the line scans were actually acquired.
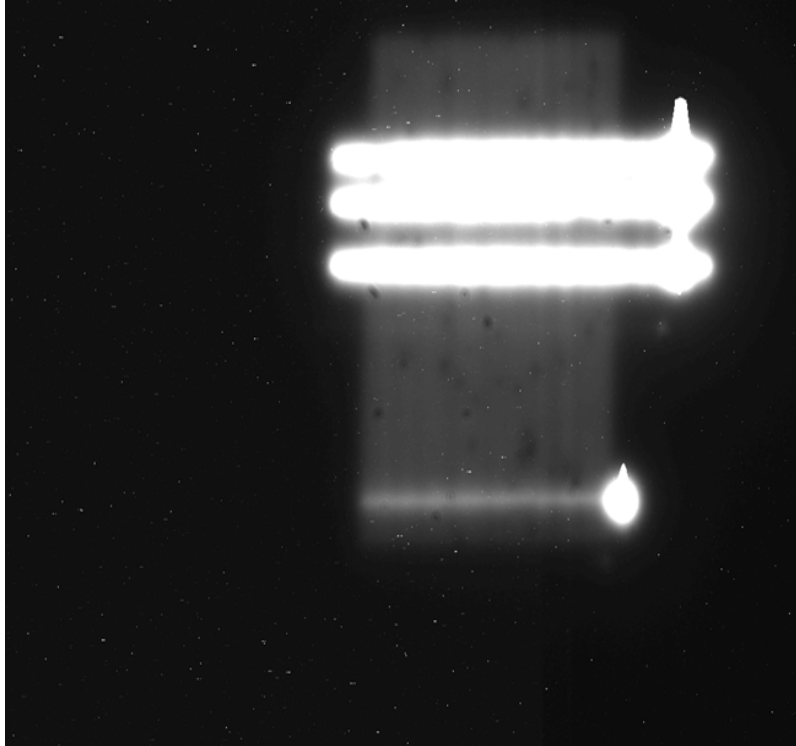
Figure 31.   Picture Mode Image Combined with Horizontal Line Images to Show Location of Line Scans on Sample (400 μm x 337 μm).

The beam energy and probe current used to create the horizontal line scan beam were 20 keV and $6x10^{-10}$ A respectively. Additionally, the SEM beam was on continuously throughout the data collection process. This eliminates any potential variation due to SEM filament differences or alignment.

Since this work is investigating the diffusion length across several dislocations, one or two line profiles from MircroCCD will not suffice or are practical since the line scan is over several hundred pixels. Therefore, a MATLAB program, contained in Appendix C, was developed to import the desired image, perform a linear regression to determine the slope of $I(x)$, extract the maximum luminescent intensity and diffusion length over the entire line scan, and then plot them on the same graph to show their relationship. Figure 32 shows the graphical results of the first horizontal line scan.
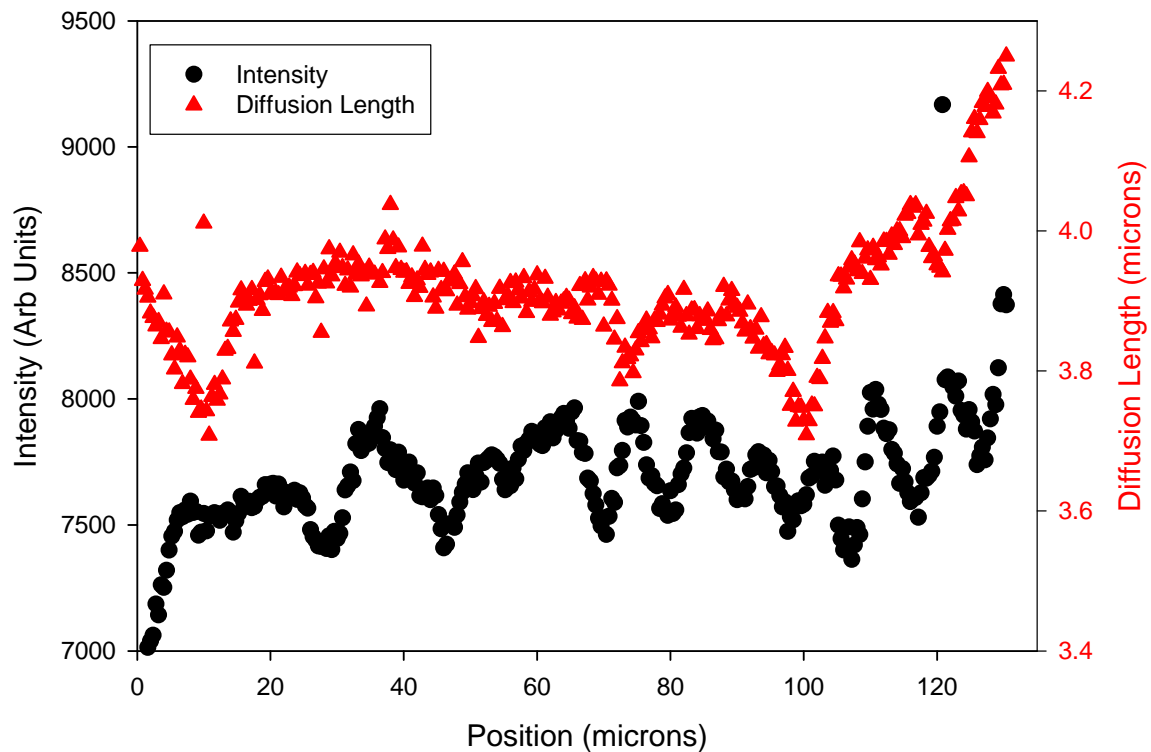
Figure 32.   Graphical Results Showing an Anti-correlation Between the Maximum
Luminescent Intensity and Diffusion Length of the Horizontal Line Scan.

Although it is not consistent across the full data set, there are obvious regions where there is an anti-correlation between the maximum luminescent intensity and the diffusion length along the horizontal line scan. A few examples of these regions are shown in Figures 33, 34, and 35. There is an approximate one to five percent variation in diffusion length spatially and these variations do not appear to be random but appear to be spatially varying in nature.
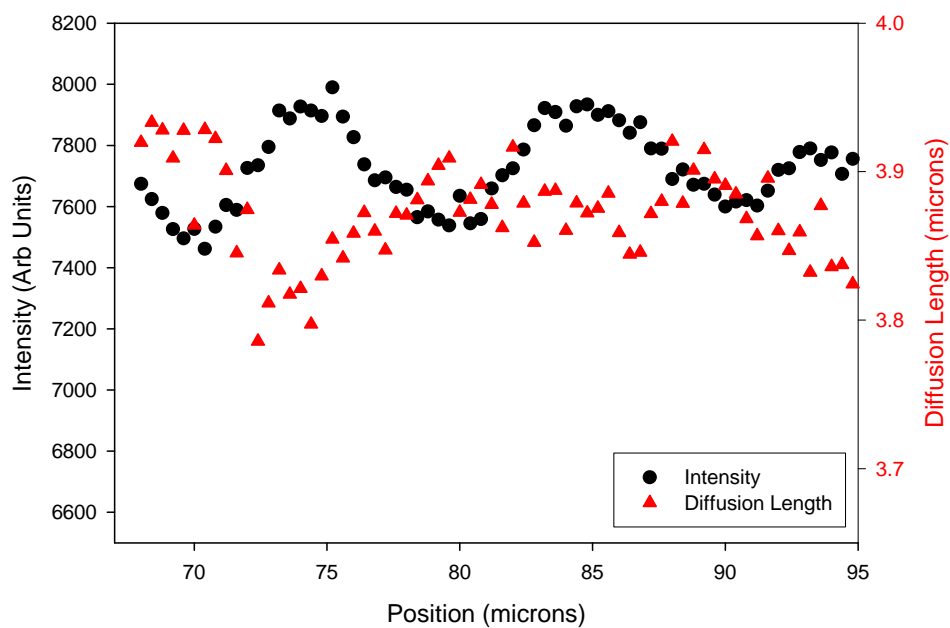
Figure 33.   Graphical Results Over a 25 Micron Region of the Horizontal Line Scan
Showing an Anti-correlation Between the Maximum Luminescent Intensity and
Diffusion Length.
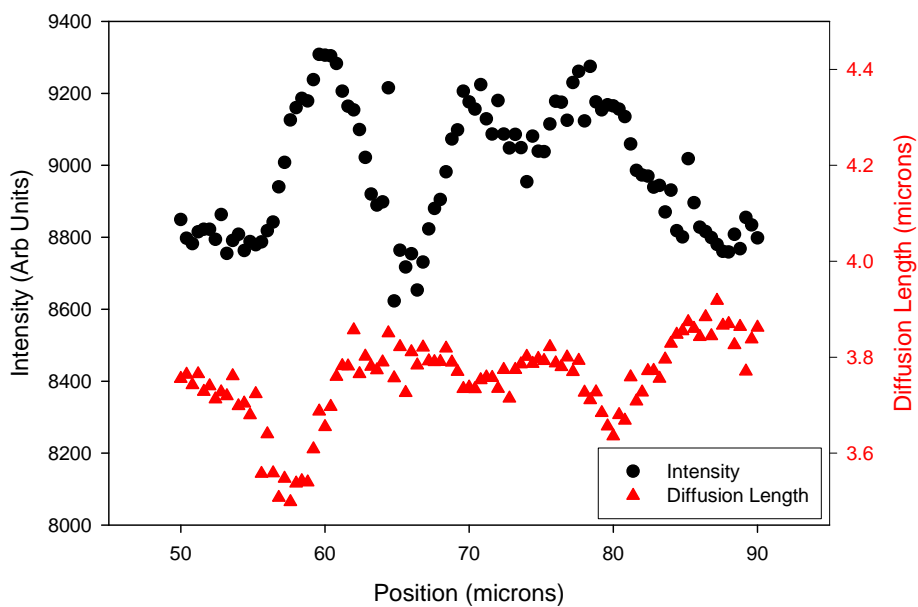
Figure 34.   Graphical Results Over a 20 Micron Region of the Horizontal Line Scan
Showing an Anti-correlation Between the Maximum Luminescent Intensity and
Diffusion Length.
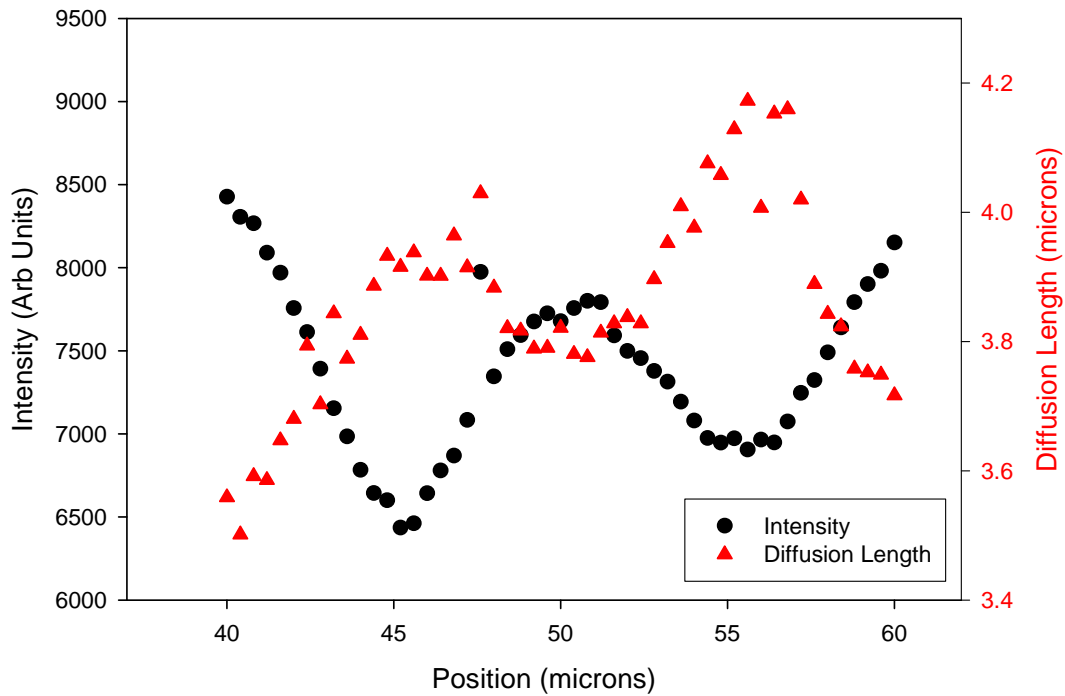
Figure 35.   Graphical Results Over a 20 Micron Region of the Horizontal Line Scan
Showing an Anti-correlation Between the Maximum Luminescent Intensity and
Diffusion Length.

To ensure that the MATLAB code was written properly and that the horizontal line scan luminescent intensity correlated with the dislocation intensity profile on the picture mode image, MicroCCD was used to extract the maximum luminescent intensity from a line profile on one of the horizontal line scans. Then the maximum luminescent intensity was extracted from a line profile on the picture mode image corresponding to the same vertical pixel value of the line profile used in the previous horizontal line scan.

Figure 36 illustrates this comparison and shows that there is a correlation between the maximum luminescence intensity in the picture mode image and the horizontal line scan image.
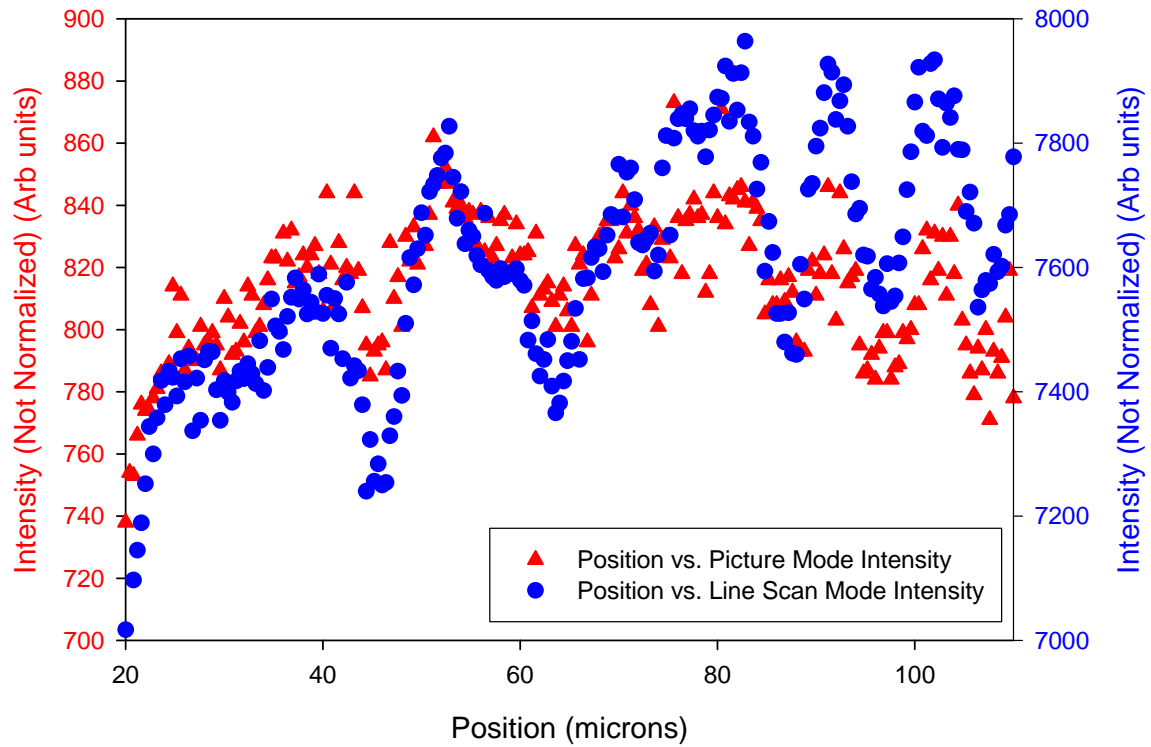
Figure 36.   Correlation Between Picture Mode Intensity and Line Scan Mode Intensity at Similar Locations on the Sample.

The difference in luminescent intensity is due to the different size areas over which the electron beam is scanned. Therefore, the variations in the horizontal line scan diffusion length across the dislocations can be analyzed and compared with the maximum luminescent intensity to correlate diffusion behavior in the light and dark bands.

2.   Discussion of Analysis

The results of the analysis on one of the horizontal line scans taken for different probe currents and scan speeds are summarized in Table 6.

Probe Current (A)/Exposure Time (sec)/Scan Speed	Light Band Intensity/ Corresponding Diffusion Length (μm)	Dark Band Intensity/ Corresponding Diffusion Length (μm)	Percent Variation of Max and Min Intensity	Percent Variation of Corresponding Diffusion Length
1e-9/10/TV	7300 / 4.42	6991 / 4.65	4.2	4.9
	7390 / 4.53	7040 / 4.67	4.7	3.0
	7346 / 4.54	7164 / 4.62	2.5	1.7
1e-9/10/Slow 1	7834 / 4.44	7583 / 4.55	3.2	2.4
	8061 / 4.64	7727 / 4.55	4.1	2.0
	8063 / 4.64	7876 / 4.53	2.3	2.4
1e-9/8/Slow 2	7676 / 4.48	7365 / 4.68	4.1	4.3
	7774 / 4.60	7434 / 4.69	4.4	1.9
	7766 / 4.56	7589 / 4.64	2.3	1.7
6e-10/20/TV	6538 / 4.38	6317 / 4.51	3.4	2.9
	6491 / 4.34	6066 / 4.46	6.5	2.7
	6590 / 4.35	6190 / 4.51	6.1	3.5
6e-10/20/Slow 1	7357 / 4.36	7127 / 4.48	3.1	2.7
	7338 / 4.36	7244 / 4.45	1.3	2.0
	7289 / 4.39	6852 / 4.47	6.0	1.8
6e-10/20/Slow 2	7517 / 4.39	7211 / 4.49	4.1	2.2
	7483 / 4.38	7353 / 4.44	1.7	1.4
	7400 / 4.39	6994 / 4.48	5.5	2.0
3e-10/50/TV	6729 / 4.18	6517 / 4.35	3.2	3.9
	6852 / 4.27	6669 / 4.47	2.7	4.5
	6646 / 4.25	6297 / 4.38	5.3	3.0
3e-10/50/Slow 1	9349 / 4.72	9091 / 4.44	2.8	6.3
	9342 / 4.27	9240 / 4.39	1.1	2.7
	9305 / 4.29	8884 / 4.45	4.5	3.6
3e-10/45/Slow 2	9276 / 4.20	8882 / 4.35	4.2	3.4
	9342 / 4.28	9080 / 4.43	2.8	3.4
	9281 / 4.28	9208 / 4.36	0.8	1.8
1e-10/180/TV	4905 / 3.79	4780 / 4.23	2.5	10.4
	5028 / 3.97	4808 / 4.31	4.4	7.9
	5133 / 4.24	4907 / 4.39	4.4	3.4
1e-10/180/Slow 1	5309 / 3.86	5162 / 4.25	2.8	9.2
	5472 / 4.10	5229 / 4.41	4.4	7.0
	5545 / 4.23	5388 / 4.56	2.8	7.2
1e-10/180/Slow 2	5712 / 3.88	5579 / 4.18	2.3	7.2
	5856 / 4.07	5583 / 4.50	4.7	9.6
	5903 / 4.14	5665 / 4.62	4.0	10.4
6e-11/300/TV	5550 / 3.82	5405 / 4.39	2.6	13.0
	5683 / 4.14	5441 / 4.46	4.3	7.2
	5821 / 4.11	5557 / 4.67	4.5	12.0
6e-11/300/Slow 1	7025 / 3.84	6469 / 4.23	7.9	9.2
	6879 / 4.07	6613 / 4.45	3.9	8.5
	7063 / 4.14	6778 / 4.73	4.0	12.5
6e-11/280/Slow 2	7452 / 3.88	7232 / 4.24	3.0	8.5
	7499 / 3.99	7181 / 4.61	4.2	13.4
	7614 / 4.12	7377 / 4.73	3.1	12.9

Table 6.   Maximum Luminescent Intensities in the Light and Dark Band and Their Corresponding Diffusion Lengths Over a 40 micron Portion of the Horizontal Line Scan (Position 1)

Tables 9 and 10 lists the results of the horizontal line scans for two additional positions and are located in Appendix A. Only a specified portion of each line scan was used due to surface imperfections that cause dark spots that indicate additional local defects. This table gives the peak luminescent intensities in the light and dark bands and the percent variations between these peak values over a length of 40 microns across each horizontal line scan. It also contains the diffusion lengths corresponding to each of the peak luminescent intensities and lists their percent variation.

The results in Figure 32 show that the peak luminescent intensities vary from 5 to 10 percent in a region of approximately 5 μm around the dislocation and the diffusion lengths vary from 1 – 7 percent in the same region. The greater the percent variation in luminescent intensity results in a greater percent variation in diffusion length. As stated earlier, these variations do not appear to be random. In some areas, there is a definite anti-correlation between the maximum luminescent intensity and the diffusion length. Since it is known that the non-radiative recombination lifetime at dislocations decrease, then it should be expected that the diffusion length would decrease in conjunction with the luminescent intensity given the assumption made earlier that $\tau_r \gg \tau_{nr}$ and applied to Equations (15) and (18) [19], [20], [21]. However, this is not the case and so an alternate explanation must be made.

The key idea is to find relationships between the maximum luminescent intensity, the minority charge carrier lifetime, and the diffusion length that match the behavior of the data that were extracted from the line scan. These relationships were derived in Chapter 2 and are represented by Equations (15), (18), and (32). However, in the limit with $\tau_r \gg \tau_{nr}$, Equation (15), $L_{diff} = \sqrt{\dfrac{\mu k T \tau_{nr}}{e}} = \sqrt{D \tau_{nr}}$ does not match the diffusion length behavior illustrated in Figure 32. Therefore, we consider the case where τ_{nr} and τ_r are comparable.

The actual equation for the minority charge carrier lifetime is given by Equation (18), $\tau = \dfrac{\tau_{rr} \tau_{nr}}{\tau_{rr} + \tau_{nr}}$. For many semiconductor materials the radiative lifetime is much

greater than the non-radiative lifetime, therefore the minority carrier effective lifetime depends only on τ_{nr}. However, the question arises when τ_r is comparable to τ_{nr} and τ_r is not constant. The minority carrier effective lifetime, determined by time resolved photoluminescence (TRPL), for this sample is listed in Table 7. The radiative recombination lifetime for low injection is determined by the equation

$$\tau_r = \frac{1}{B \square N} = \frac{1}{B \square p} \qquad (35)$$

where p is the free hole concentration and the B-coefficient is the coefficient for radiative recombination determined by band theory. Knowing these two variables the radiative lifetime can be calculated using Equation (35). Equation (18) can then be used to solve for the total non-radiative lifetime. All of the known values and the results of the calculations are listed in Table 7.

$In_{49}Ga_{51}P$ Variable Values	
Free Carrier Concentration	$1e^{17}$ cm^{-3}
B-coefficient	$2.41e^{-10}$ cm$^3/s$
Radiative Lifetime	37.7 ns
Effective Lifetime	13.1 ns
Non-Radiative Lifetime	20.1 ns

Table 7. Known and Calculated Lifetimes for the $In_{49}Ga_{51}P$ Sample.

The values in Table 7 represent the average different lifetime mechanisms over the entire sample and show that the radiative lifetime is comparable to the non-radiative lifetime. Figure 37 was produced by work done in [31] by using a form of Equation (16) and contains theoretical curves that show minority carrier lifetime as a function of dislocation density for a sample with a specific dopant concentration.
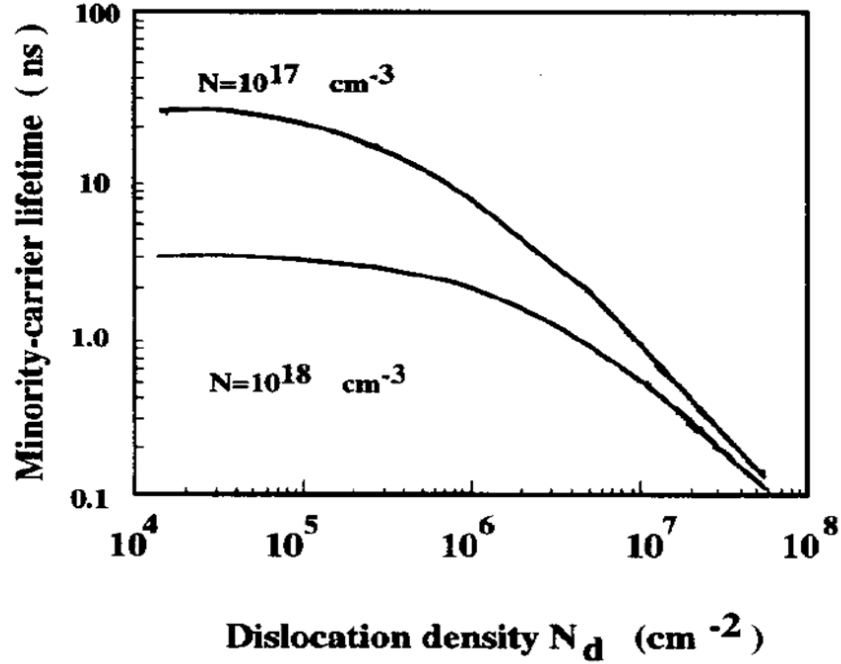
Figure 37.   Theoretical Values Calculated Using Equation (18), N is the Majority Carrier Concentration [From: 31].

The dislocation density for $In_{49}Ga_{51}P$ grown on a Germanium (Ge) substrate, which was the sample used in this work, was determined as shown in Figure 35.

The dislocation density was determined by first finding the pixel area of the image. Then the area in microns was found by multiplying the pixel area with the square of the fixed resolution of the optical microscope and CCD camera which is 0.4 $\mu m/pixel$. The number of dislocation lines for the area was obtained by first counting the number of vertical dark bands perpendicular to the intensity line profile represented in red and shown in Figure 38. Using the fact that there are dark bands in both the horizontal and vertical directions that are perpendicular to each other, the number of dark bands determined vertically can be squared to give the number of dark bands in the area of the intensity line profile. From this information the average dislocation density per unit area was determined to be $\delta_{xy} = 6.24x10^{-3}$ area/$(\mu m)^2 = 6.24x10^5$ area/cm^2.
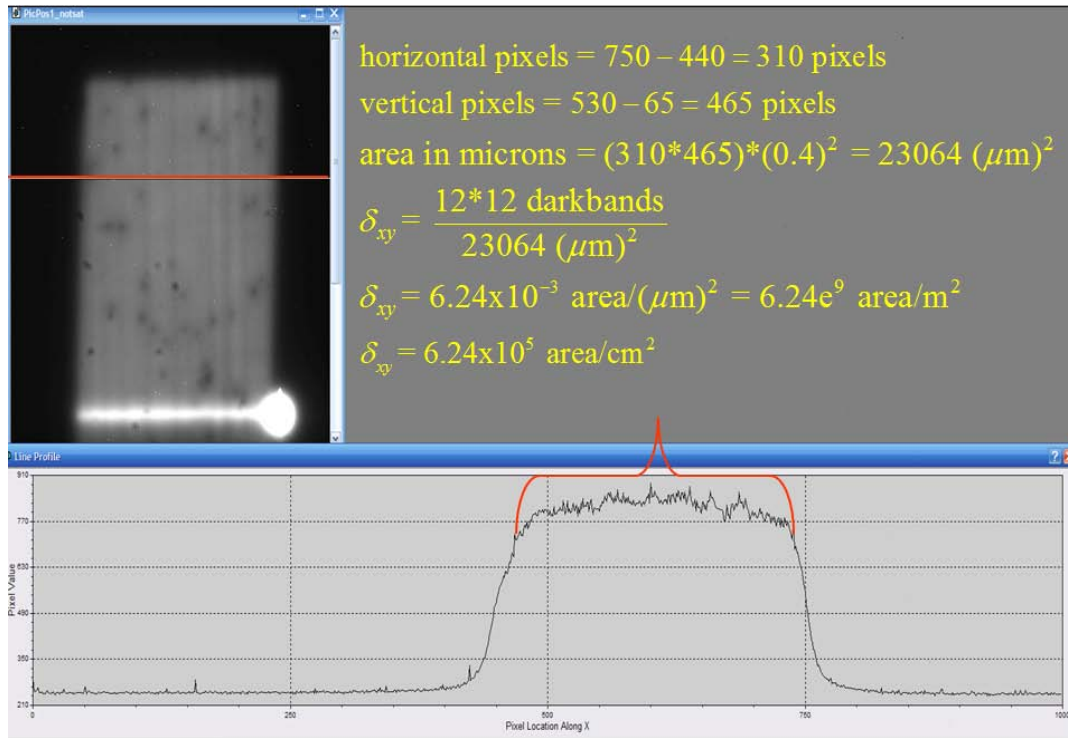
Figure 38.   Derivation and Calculation of the Dislocation Density Using a Line Profile.

Using the theoretical curves in Figure 37, the dopant concentration listed in Table 7, and the dislocation density calculated in Figure 38, the accuracy to within the same order of magnitude of the measured value of the effective minority carrier lifetime determined by TRPL was verified to within a 8.4 percent difference or a factor of 1.09. This difference can be explained by the fact that the dislocation density was just an approximate calculation and therefore maybe actually slightly less. A smaller dislocation density would give a larger minority carrier lifetime based on the theoretical curves in Figure 37. The results are listed in Table 8.

66

Material	Effective Lifetime (TRPL) (ns)	Approximate Effective Lifetime from Figure 34. (ns)	Percent Variation (%)	Factor Difference
InGaP/Ge	13.1	12	8.4	1.09

Table 8.   Comparison of Measured Effective Minority Carrier Using Lifetime Using TRPL and Theoretical Values Calculated Using Equation (16) [31].

Now that it is known that the radiative and non-radiative lifetimes are comparable, it is time to show that they both vary spatially. Referring back to the graph in Figure 37, it can be seen that the effective minority carrier lifetime varies with respect to dislocation density. Therefore, it can be surmised that either just the non-radiative lifetime decreases due to deeper impurity levels or that both the radiative and non-radiative lifetimes vary. If the non-radiative lifetime decreases due to defect states associated with the dislocations, as is known to be true, then the radiative lifetime will increase if the Fermi level moves toward the center of the gap and reduces the free hole population. The mechanism for this increase in radiative lifetime is the fact that near the dislocations the majority charge carrier or hole concentration is slightly reduced, thus further decreasing the chances of a minority charge carrier recombination. Equation (35) represents the relationship between the hole concentration and the radiative lifetime. With these ideas in mind and applied to Equations (15) and (31) we get the relationships

$$L_{diff} = \sqrt{\frac{\mu k T \tau}{e}} = \sqrt{D \frac{\tau_r \tau_{nr}}{\tau_r + \tau_{nr}}} \tag{36}$$

and

$$I_{max} \approx \frac{g}{2\tau_r} \frac{\tau_r \tau_{nr}}{\tau_r + \tau_{nr}} \approx \frac{g \Box \tau_r \tau_{nr}}{2\tau_r^2 + 2\tau_r \tau_{nr}} \tag{37}$$

with all variables as previously defined. A model was constructed with simulated variations in τ_{nr} and τ_r to determine if this would reproduce the experimental results. Equations (35), (36), and (37) were used in the model with the non-radiative lifetime and the hole concentration being the variables.   The non-radiative lifetime and hole

concentration was decreased by a periodic cosine function to simulate the effects of the dislocation regions. Therefore, both the non-radiative lifetime and hole concentration would decrease to a point and then begin to increase simulating a light band region. Figure 39 illustrates the modeled relationship between the free hole concentration and the radiative lifetime. The simulation shows a significant decrease of approximately 50 percent in the hole concentration.
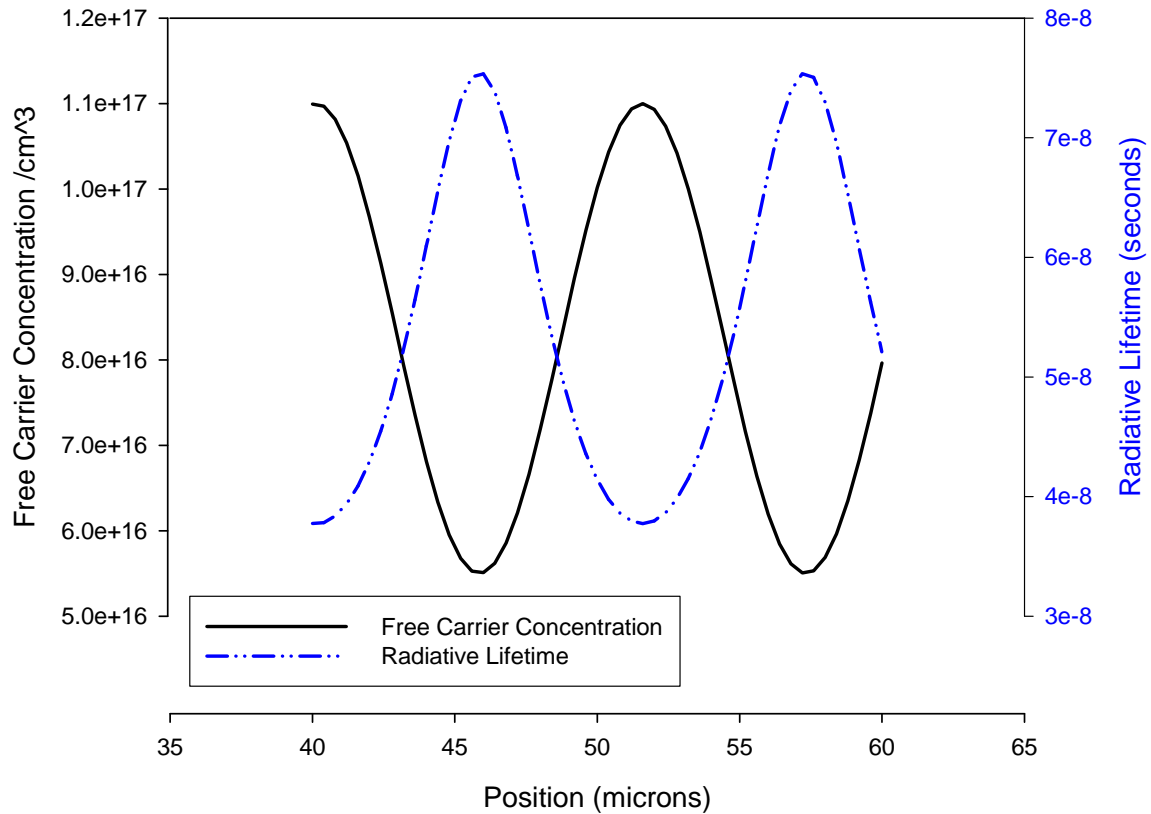
Figure 39.   Modeled Results Showing the Relationship Between the Dopant Concentration and the Radiative Lifetime Across Two Simulated Dark Bands.

The experimental and modeled results for one simulated dark and light band are listed in Table 11 in Appendix B and are illustrated with the experimental data over a length of 40 microns across the horizontal line scan in Figures 40 and 41.
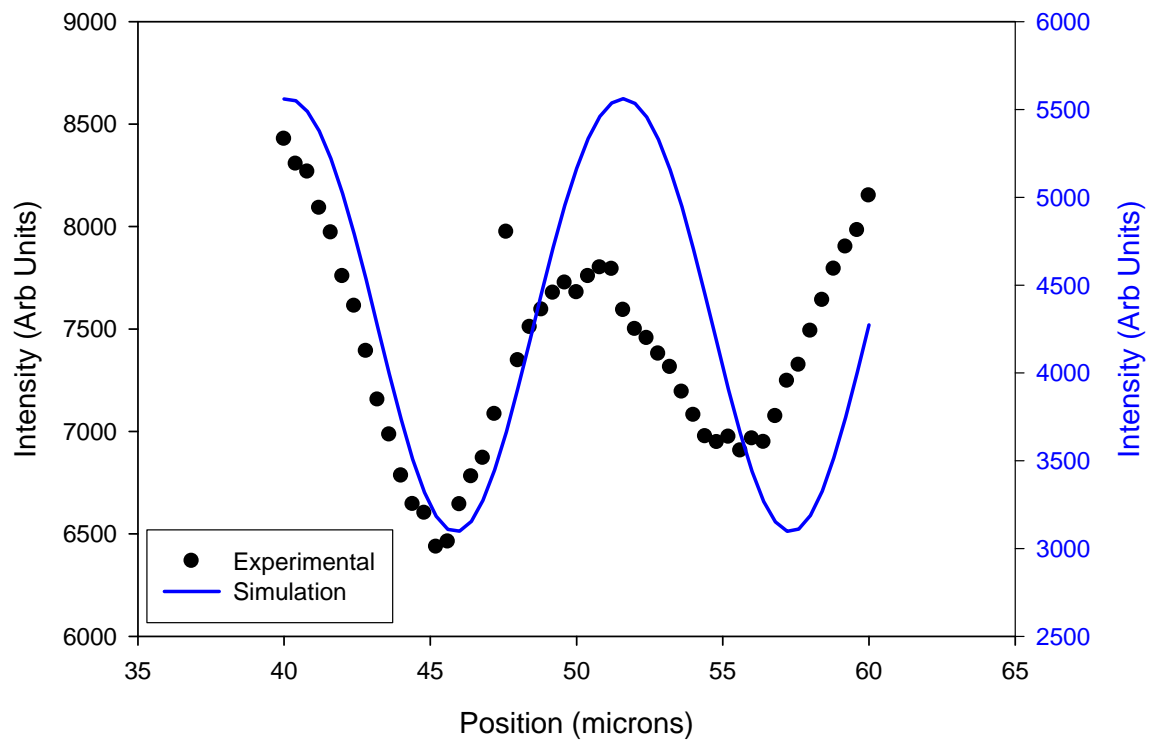
Figure 40.   Experimental and Modeled Results of the Maximum Luminescent Intensity
across a 40 Micron Length of the Horizontal Line Scan.
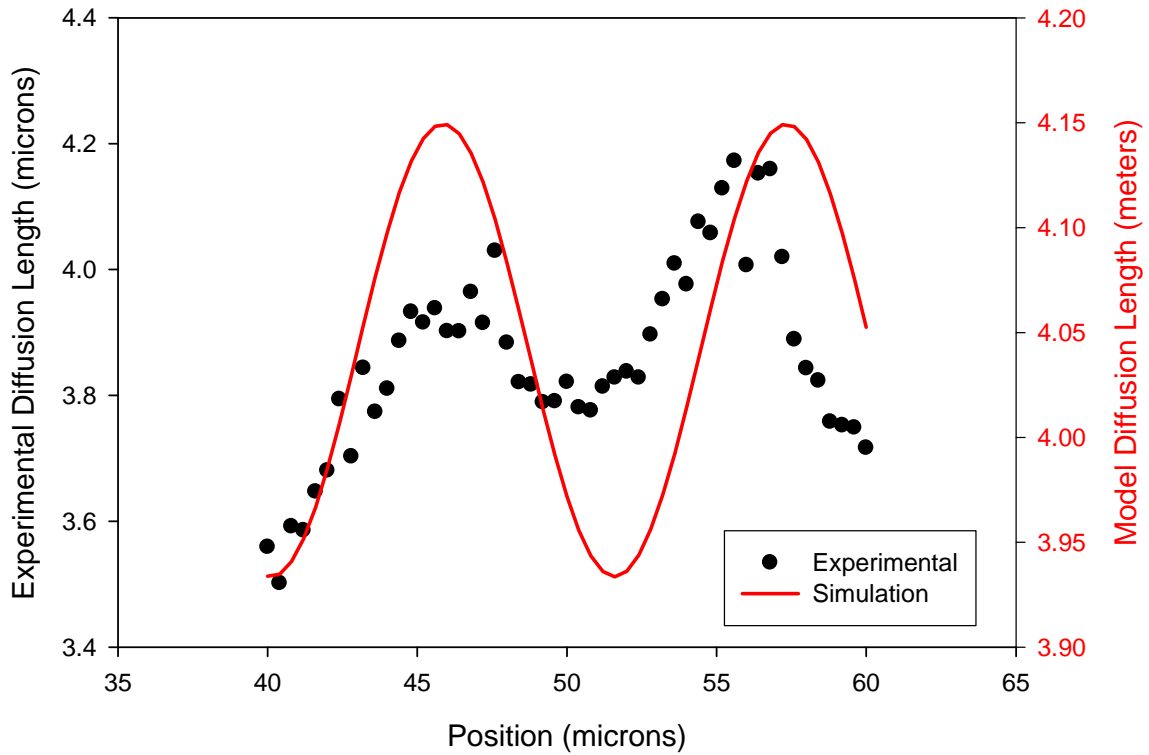
Figure 41.   Experimental and Modeled Results of the Diffusion Length across a 40
Micron Length of the Horizontal Line Scan.

In addition, the simulated data resulted in a percent variation in diffusion length and intensity that was within the ranges comparable to that of the experimental data. Therefore, the simulated results show that it is possible for the diffusion length to increase in the dark bands, due to the increase in radiative lifetime, which causes an overall increase in effective lifetime.

3.   Final Observations

Now that a working model has been created simulating the experimental results and validating Equations (35), (36), and (37), there is another interesting idea that is important to mention. In addition to the qualitative behavior of the various lifetime mechanisms and the measurement of the diffusion length in the material, the quantum efficiency is also a very important and critical measurement in solar cell construction.

70

The quantum efficiency is a measure of the current that a solar cell will produce when illuminated by light at a particular wavelength. In other words it is a percent measure of how many electron-hole pairs are created when a photon hits the surface of the material. Thus, the more electron-hole pairs that are produced, in turn allow more electrons to be available to move through the circuit and create more current, thus increasing quantum efficiency. The quantum efficiency can be calculated if the effective lifetime and the radiative lifetime are known by using the equation

$$\eta = \frac{\tau_{eff}}{\tau_r} \tag{38}$$

where η is the quantum efficiency and all other variables are as previously defined. Equation (38) shows that for the analysis conducted in this work on the $In_{49}Ga_{51}P$ sample, as the radiative lifetime increases due to the effects of the dislocations on the free hole concentration then the quantum efficiency will decrease. This is also due to the fact that the radiative minority carrier lifetime increases more than the effective lifetime at the dislocations. Figure 42 shows the relationship from the simulation between the effective and radiative lifetimes. Figure 43 then illustrates how they affect the behavior of the quantum efficiency. As expected, the quantum efficiency decreases in the dislocations and since this behavior was successfully illustrated in the simulation, more credibility is given to the results of the simulated behaviors.
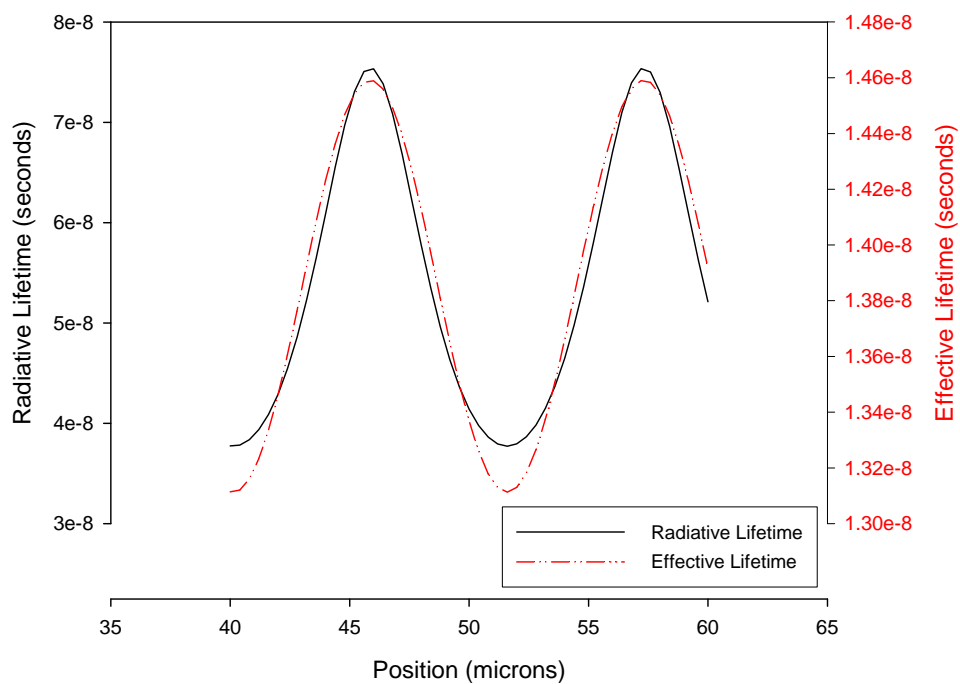
Figure 42.   Simulated Graph of the Radiative and Effective Minority Carrier Lifetimes.
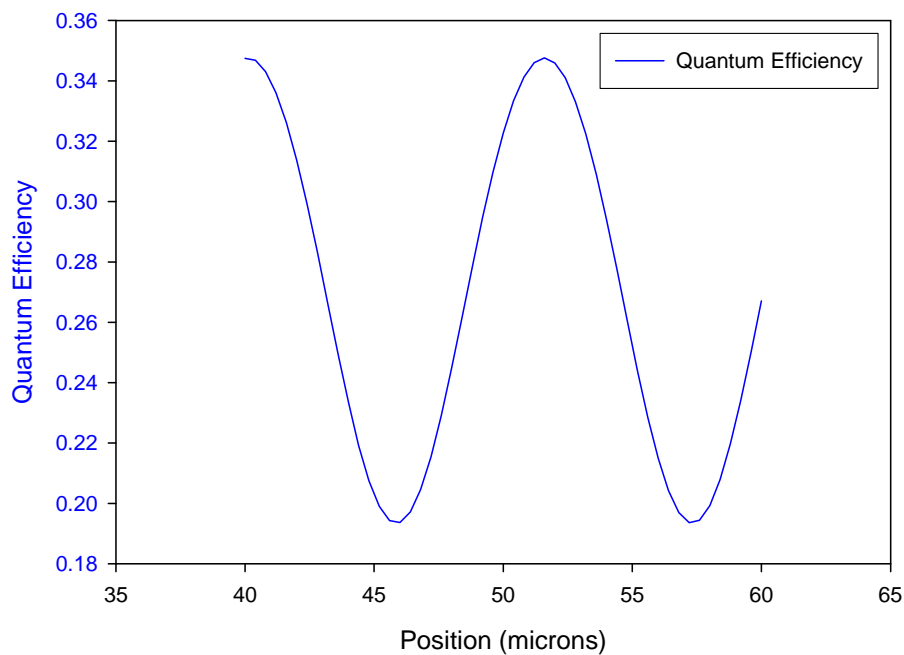
Figure 43.   Simulated Graph of the Effects of Radiative and Effective Minority Carrier
Lifetimes on the Quantum Efficiency.

V. CONCLUSION AND SUGGESTIONS FOR FURTHER RESEARCH

A. CONCLUSION AND SUMMARY

Using the technique developed to quantitatively and non-destructively extract the minority carrier diffusion lengths from spatially resolved luminescence, the variations in diffusion length and maximum luminescent intensity were able to be measure. The values of the diffusion length were able to be measured to within 0.1 microns and differed between less than a percent to five percent across the dislocation bands. Also, a model was successfully developed to simulate and explain the anti-correlating behavior discovered between the maximum luminescent intensity and the diffusion length across dislocation bands in a sample of $In_{49}Ga_{51}P$ material. In addition, the simulation was also able to reproduce the light to dark band behavior seen in the maximum luminescent intensities and the diffusion lengths.

Originally, it was assumed that in the low injection limit $\tau_r >> \tau_{nr}$ and $\tau_r = \text{constant}$ for this material. When these assumptions were applied to the equations for intensity and diffusion length, the experimental data collected from the SEM did not match the theoretical relationships. The effective minority charge carrier lifetime was known from TRPL and the radiative lifetime could be calculated, therefore the non-radiative lifetime was also calculated revealing that the radiative and non-radiative lifetimes were comparable. In addition, the non-radiative lifetime is known to decrease at dislocation sites due to deep level defects located there. The increased concentration of defect sites cause the free hole concentration to decrease near the dislocation thereby increasing the radiative lifetime. Using these new relationships established between the minority carrier lifetime mechanisms and the free hole concentration, the model was able to reproduce the experimental results showing an increase in effective lifetime in the regions of lower luminescence.

In conclusion, the model furthers understanding of the behavior of the radiative and non-radiative recombination mechanisms and how they affect the luminescent intensity and diffusion length within the dislocations. The model also shows how dislocation areas affect the free hole concentrations and how that in turn affects the radiative lifetime. Finally, and probably one of the most important aspects of a solar cell is that if the radiative lifetime increases more than the effective minority carrier lifetime then according to the quantum efficiency equation, the quantum efficiency or production of electron-hole pairs decrease at the dislocation site. Therefore, the development of improved solar cell growth techniques needs to minimize the dislocations at the lattice interfaces thus increasing quantum efficiency and improving total current production.

B.   SUGGESTIONS FOR FURTHER RESEARCH

1.   Analysis of Crystallographic Directionality on Diffusion Length Variations and Minority Carrier Lifetime Behavior

At the beginning of Chapter IV, the horizontal line scan was introduced and described as the SEM mode that was used to extract the maximum luminescent intensity and diffusion length across the dislocation bands in Figure 14. However, it has been seen in the triple junction solar cell material, such as InGaAs, that there are two sets of dislocation bands that are perpendicular to one another. The sample of $In_{49}Ga_{51}P$ used in this work has dislocation bands that are very distinct in one direction, however, the second set of perpendicular bands are not as visible in the SEM images. The existence of these perpendicular bands can be identified by rotating the horizontal line scan 90 degrees to create a vertical line scan. Figure 44 shows a combined image of the picture mode of the general location on the sample and a vertical line scan image that was taken in order to extract the luminescent intensities and diffusion lengths along a horizontal line profile.
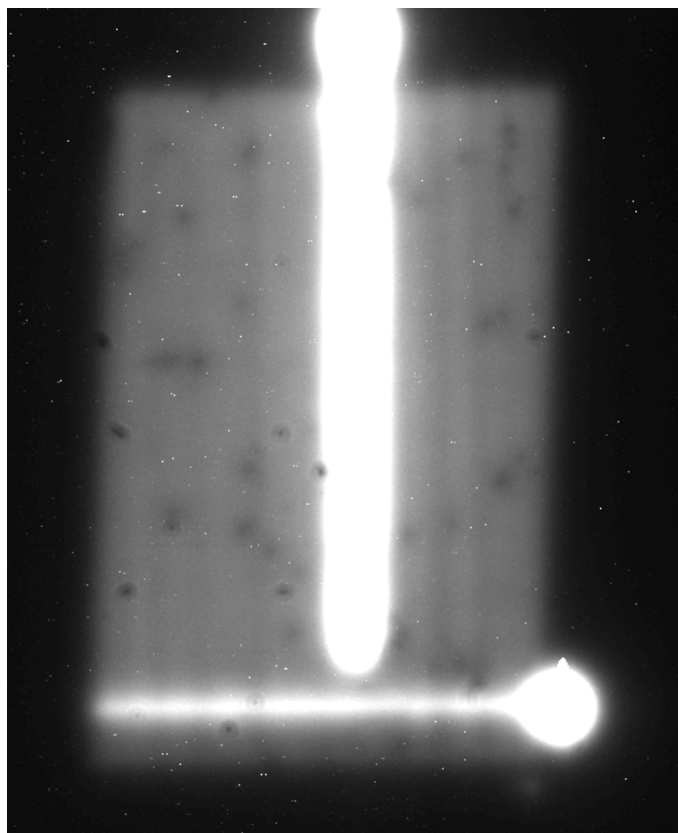
Figure 44.   Combined Image of the Picture Mode and the Vertical Line Scan Mode
Showing the Location of the Line Scan Beam.
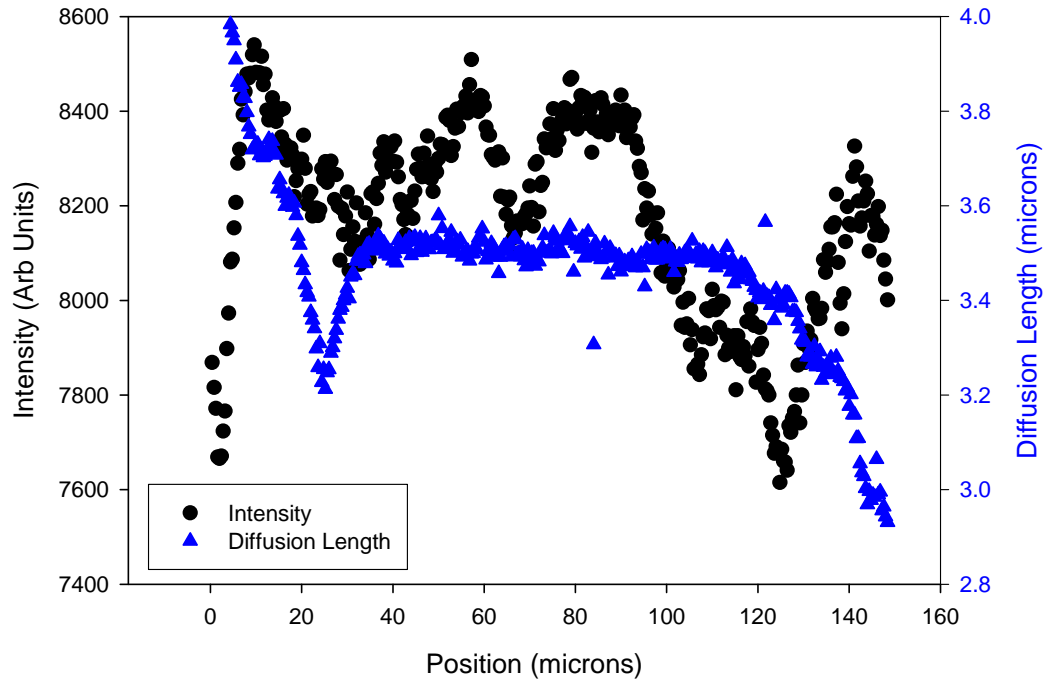
Figure 45.   Maximum Luminescent Intensity and Diffusion Length Results for a Vertical
Line Scan Along a Dislocation Band.

The graphical results, shown in Figure 45, are similar to the graphical results obtained
from the horizontal line scan.   Since the behavior of the luminescent intensities and
diffusion lengths are similar as previously determined, the technique and simulation
developed in this thesis should be able to be applied in this instance as well.   Therefore,
more analysis should be conducted to determine and compare the spatial variations of
diffusion length due anisotropy and to expand this analysis to other triple junction solar
cell material such as InGaAs.   The simulation should then be applied to these analyses to
qualitatively determine if the behavior of the diffusion length and the various lifetimes
are consistent in all cases.

2. Effects of Varying Solar Cell Material Properties on Diffusion Length and Minority Carrier Lifetime Behavior

Figure 46 shows a SEM picture mode image of a sample of *InGaAs* grown on a GaAs substrate. The picture clearly illustrates the importance of lattice matching when growing a material on a particular substrate. The lattice constants of these two materials vary by about four percent, which results in the distinct vertical and horizontal dislocation bands seen in the image.
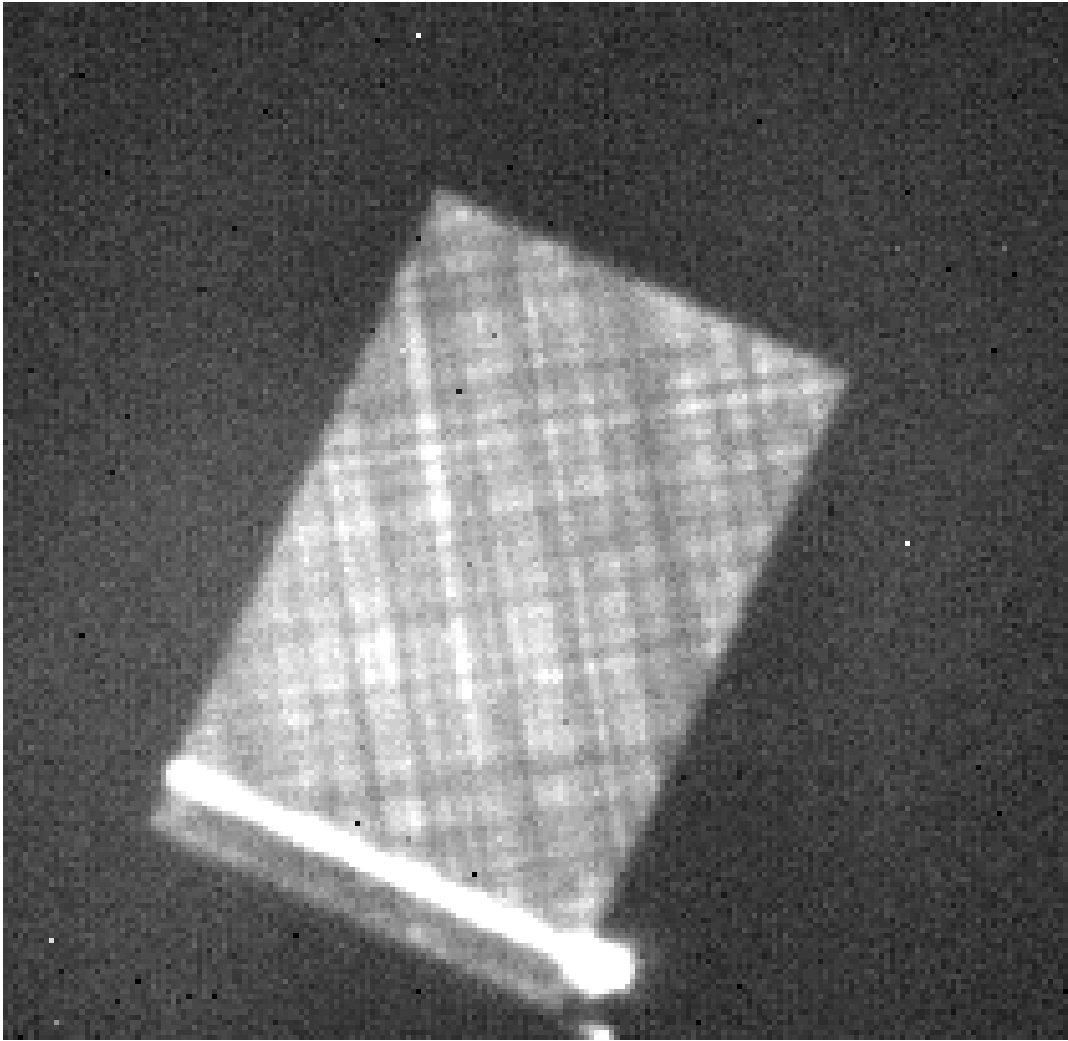
Figure 46.   A SEM Picture Mode Image of a Sample of InGaAs Grown on a GaAs Substrate (204 μm x 204 μm) and Showing the Horizontal and Vertical Dislocation Bands.

Figure 47 shows the variations in maximum luminescent intensity which appear to be between 10 – 20 percent, however, the variations in the diffusion length were approximately one to two percent higher than the variations in the diffusion lengths for $In_{49}Ga_{51}P/Ge$, which as described in Chapter II has a lattice constant difference of less than a tenth of a percent.
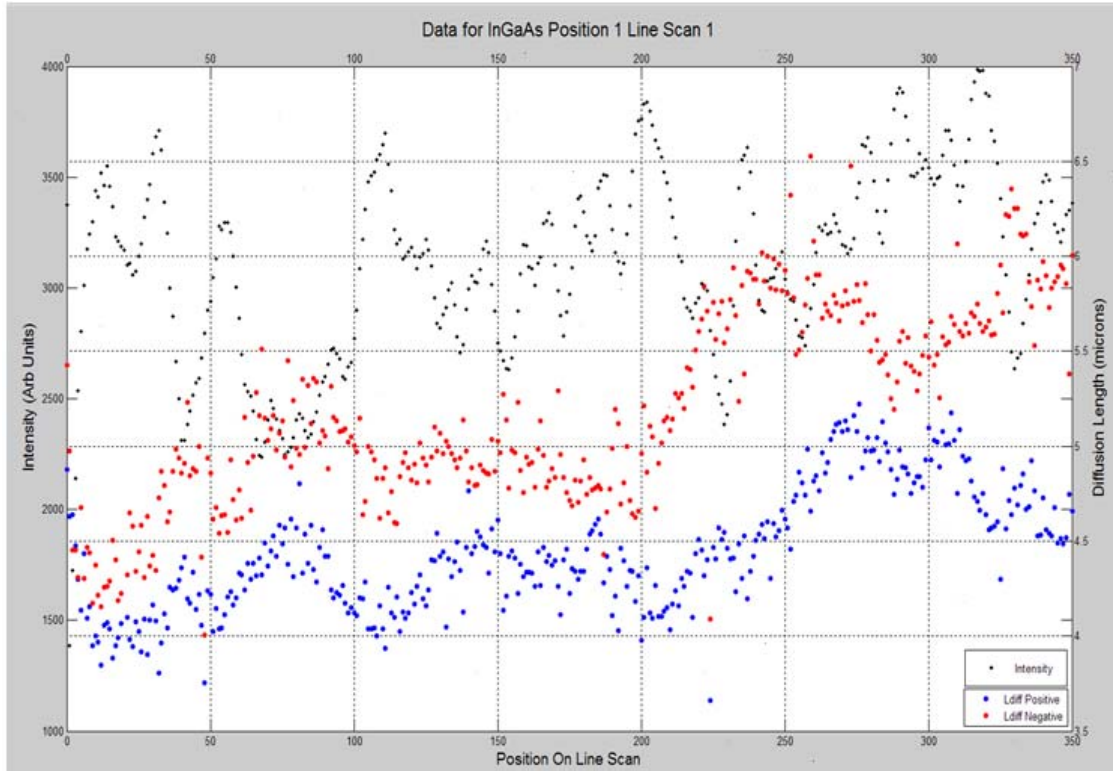
Figure 47.   Results from a Vertical Line Scan on a Sample of InGaAs Showing the Same Anti-correlating Behavior Between the Diffusion Length and the Maximum Luminescent Intensity.

Current research is investigating the possibility of making more efficient solar cells by growing non-lattice matched materials. This is used to tune the band-gap in these materials. However, even if the band-gap is tuned to get better recombination between electrons and holes, it still does not solve the problem of the dislocations affecting the free hole concentration and thus increasing the radiative lifetime thereby decreasing quantum efficiency. More investigation should be conducted by comparing lattice

matched and non-lattice matched solar cell samples of varying mole concentrations, atomic ordering, and doping concentrations to determine their effects on the various minority charge carrier lifetime mechanisms and how that in turn affects the quantum efficiency and diffusion length, which are key parameters in constructing highly efficient solar cell material.

THIS PAGE INTENTIONALLY LEFT BLANK

APPENDIX A.   DATA TABLES FOR THE LINE SCAN RESULTS

Probe Current (A)/Exposure Time (sec)/Scan Speed	Light Band Intensity/ Corresponding Diffusion Length (μm)	Dark Band Intensity/ Corresponding Diffusion Length (μm)	Percent Variation of Max and Min Intensity	Percent Variation of Corresponding Diffusion Length
1e-9/10/TV	7202/3.85	6844/3.98	5.0	3.3
	7147/3.92	6958/4.14	2.6	5.3
	7005/4.02	6866/4.10	2.0	2.0
1e-9/10/Slow 1	8310/3.84	7972/3.99	4.1	3.8
	8327/3.87	8021/4.12	3.7	6.1
	8260/4.02	8050/4.10	2.5	2.0
1e-9/8/Slow 2	8704/3.85	8337/4.01	4.2	4.0
	8781/3.92	8441/4.10	3.9	4.4
	8668/4.01	8531/4.07	1.6	1.5
6e-10/20/TV	9238/3.76	8868/3.90	4.0	3.6
	9271/3.81	8909/3.98	3.9	4.3
	9025/3.92	8885/3.99	1.6	1.8
6e-10/20/Slow 1	9537/3.58	9100/4.04	4.6	11.4
	9229/3.91	8589/4.15	6.9	5.8
	9348/3.94	8919/4.07	4.6	3.2
6e-10/20/Slow 2	8981/3.60	8470/3.99	5.7	9.8
	8660/3.92	8248/4.13	4.8	5.1
	8784/3.92	8527/4.03	2.9	2.7
3e-10/50/TV	7242/3.59	6942/3.72	4.1	3.5
	7278/3.61	6985/3.84	4.0	6.0
	7192/3.69	6978/3.89	3.0	5.1
3e-10/50/Slow 1	8563/3.70	8205/3.89	4.2	4.9
	8355/3.75	8115/3.90	2.9	3.8
	8524/3.57	8165/3.88	4.2	8.0
3e-10/45/Slow 2	8554/3.51	8035/3.90	6.1	10.0
	8202/3.84	7779/3.99	5.2	3.8
	8474/3.79	8114/3.91	4.2	3.1
1e-10/180/TV	6117/3.35	5910/3.49	3.4	4.0
	6099/3.23	5858/3.63	4.0	11.0
	5972/3.47	5725/3.74	4.1	7.2
1e-10/180/Slow 1	6577/3.35	6461/3.51	1.8	4.6
	6793/3.32	6499/3.57	4.3	7.0
	6610/3.48	6451/3.59	2.4	3.1
1e-10/180/Slow 2	7751/3.43	7456/3.5	3.8	2.0
	7858/3.38	7505/3.63	4.5	6.9
	7721/3.45	7549/3.65	2.2	5.5

Table 9.   Maximum Luminescent Intensities in the Light and Dark Band and Their Corresponding Diffusion Lengths Over a 40 micron Portion of the Horizontal Line Scan (Position 2).

Probe Current (A)/Exposure Time (sec)/Scan Speed	Light Band Intensity/ Corresponding Diffusion Length (μm)	Dark Band Intensity/ Corresponding Diffusion Length (μm)	Percent Variation of Max and Min Intensity	Percent Variation of Corresponding Diffusion Length
1e-9/10/TV	8056/3.53	7483/3.89	7.1	9.3
	7972/3.78	7798/3.87	2.2	2.3
	7955/3.67	7535/3.97	5.3	7.6
1e-9/10/Slow 1	9276/3.49	8614/3.90	7.1	10.5
	9233/3.81	9007/3.88	2.4	1.8
	9196/3.63	8720/3.95	5.2	8.1
1e-9/8/Slow 2	9472/3.54	8997/3.92	5.0	9.7
	9543/3.79	9341/3.90	2.1	2.8
	9528/3.65	9147/3.94	4.0	7.4
6e-10/20/TV	9308/3.50	8623/3.85	7.4	9.1
	9224/3.73	8954/3.82	2.9	2.4
	9168/3.64	8759/3.92	4.5	7.1
6e-10/20/Slow 1	8831/3.50	8377/3.87	5.1	9.6
	8748/3.72	8405/3.80	3.9	2.1
	8745/3.61	8259/3.87	5.6	6.7
6e-10/20/Slow 2	8931/3.50	8293/3.83	7.1	8.6
	8908/3.73	8579/3.81	3.7	2.1
	8895/3.63	8442/3.87	5.1	6.2
3e-10/50/TV	7006/3.40	6331/3.67	9.6	7.4
	6749/3.58	6571/3.66	2.6	2.2
	6691/3.49	6289/3.71	6.0	5.9
3e-10/50/Slow 1	8768/3.41	8033/3.69	8.4	7.6
	8514/3.58	8266/3.69	2.9	3.0
	8540/3.53	7993/3.74	6.4	5.6
3e-10/45/Slow 2	9039/3.51	8217/3.70	9.1	5.1
	8804/3.56	8539/3.64	3.0	2.2
	8828/3.55	8268/3.69	6.3	3.8
1e-10/180/TV	5202/3.20	4771/3.50	8.3	8.6
	5080/3.24	4953/3.49	2.5	7.2
	5041/3.25	4794/3.56	4.9	8.7
1e-10/180/Slow 1	7335/3.63	6817/3.78	7.1	4.0
	7151/3.66	7047/3.76	1.5	2.7
	7148/3.64	6694/3.82	6.4	4.7
1e-10/180/Slow 2	8623/3.68	8062/3.78	6.5	2.6
	8461/3.70	8281/3.77	2.1	1.9
	8497/3.70	7899/3.81	7.0	2.9
6e-11/300/TV	7433/3.58	6936/3.78	6.7	5.3
	7385/3.69	7201/3.76	2.5	1.9
	7316/3.66	6898/3.87	5.7	5.4
6e-11/300/Slow 1	7378/3.57	6815/3.79	7.6	5.8
	7230/3.63	7050/3.72	2.5	2.4
	7190/3.63	6863/3.80	4.5	4.5
6e-11/280/Slow 2	7779/3.51	7114/3.70	8.5	5.1
	7465/3.58	7302/3.64	2.2	1.6
	7454/3.57	7012/3.74	5.9	4.5

Table 10. Maximum Luminescent Intensities in the Light and Dark Band and Their Corresponding Diffusion Lengths Over a 40 micron Portion of the Horizontal Line Scan (Position 3).

APPENDIX B.   DATA TABLE FOR THE SIMULATED RESULTS

Free Hole Concetration (cm^{-3})	Radiative Lifetime (ns)	Non-radiative Lifetime (ns)	Diffusion Length Sim (microns)	Diffusion Length Exp. (microns)	Intensity Sim. (Arb Units)	Intensity Exp. (Arb Units)
1.10e17	37.7	20.1	3.93	3.56	5559	8427
1.10e17	37.8	20.1	3.93	3.50	5550	8305
1.08e17	38.4	20.0	3.94	3.59	5489	8267
1.05e17	39.4	19.9	3.95	3.59	5377	8090
1.02e17	40.9	19.8	3.97	3.65	5220	7970
9.67e16	42.9	19.6	3.99	3.68	5021	7757
9.13e16	45.5	19.4	4.01	3.79	4789	7612
8.54e16	48.6	19.2	4.03	3.70	4533	7392
7.94e16	52.3	19.0	4.05	3.84	4263	7154
7.35e16	56.4	18.8	4.08	3.77	3993	6984
6.81e16	60.9	18.6	4.10	3.81	3737	6784
6.33e16	65.5	18.4	4.12	3.89	3508	6644
5.95e16	69.7	18.3	4.13	3.93	3320	6601
5.68e16	73.1	18.2	4.14	3.92	3184	6436
5.53e16	75.1	18.1	4.15	3.94	3109	6462
5.51e16	75.3	18.1	4.15	3.90	3099	6643
5.62e16	73.8	18.1	4.14	3.90	3155	6780
5.86e16	70.8	18.2	4.14	3.96	3273	6870
6.21e16	66.8	18.3	4.12	3.91	3447	7084
6.66e16	62.3	18.5	4.10	4.03	3665	7974
7.18e16	57.8	18.7	4.08	3.88	3914	7346
7.76e16	53.5	18.9	4.06	3.82	4182	7509
8.36e16	49.6	19.1	4.04	3.82	4453	7594
8.96e16	46.3	19.4	4.01	3.79	4714	7676
9.52e16	43.6	19.6	3.99	3.79	4955	7725
1.00e17	41.4	19.7	3.97	3.82	5164	7678
1.04e17	39.8	19.9	3.96	3.78	5335	7757
1.07e17	38.6	20.0	3.94	3.78	5460	7800
1.09e17	37.9	20.1	3.94	3.81	5537	7792
1.10e17	37.7	20.1	3.93	3.83	5562	7592
1.09e17	38.0	20.1	3.94	3.84	5535	7499
1.07e17	38.7	20.0	3.94	3.83	5456	7455
1.04e17	39.8	19.9	3.96	3.90	5329	7379
1.00e17	41.5	19.7	3.97	3.95	5157	7314
9.50e16	43.7	19.6	3.99	4.01	4946	7193
8.93e16	46.4	19.3	4.01	3.98	4705	7080
8.34e16	49.8	19.1	4.04	4.08	4442	6975
7.74e16	53.6	18.9	4.06	4.06	4171	6947
7.16e16	57.9	18.7	4.08	4.13	3904	6973
6.64e16	62.5	18.5	4.10	4.17	3656	6906
6.19e16	67.0	18.3	4.12	4.01	3439	6965
5.85e16	71.0	18.2	4.14	4.15	3268	6948
5.61e16	73.9	18.1	4.14	4.16	3151	7074
5.51e16	75.4	18.1	4.15	4.02	3098	7246
5.53e16	75.0	18.1	4.15	3.89	3110	7324

Table 11. The Experimental and Simulated results for One Dark and Light Band.

THIS PAGE INTENTIONALLY LEFT BLANK

APPENDIX C.   HORIZONTAL LINE SCAN MAXIMUM LUMINSCENT INTENSITY AND DIFFUSION LENGTH EXTRACTION MATLAB CODE (WRITE_HORIZONTAL.M AND READDATA_HORIZONTAL_UPDATED.M)

```matlab
%WRITEDATA_HORIZONTAL.M
clear all
clc
rin=4;
rout=12;
I = imread('HorizLineScan3_6e-11_Slow2.tif');
I = double(I);
yx = size(I);
xx=linspace(1,yx(2),yx(2));
yy=linspace(1,yx(1),yx(1));
[X Y]=meshgrid(xx,yy);
contour(X,Y,I)
axis equal
axis ([0 max(yx) 0 max(yx)])
y = [1 842];
s = 375;
t = 725;
for n = s:t    %750 is the max
        x = [n n];
        [Cx Cy C] = improfile(I,x,y);
        A = [Cy C];
        [IntMax PosMax] = max(A);
[IntMax] = min(IntMax);
[Poscenter] = min(PosMax);
yyy = Cy(1:841);    %This is using the actual pixel values from
improfile
%                   command
ymicron = .4*(yyy-Poscenter);
ylinenorm = (C-mean(C(2:30)))/(IntMax-mean(C(2:30)));
yx = size(I);
mm=1;
for m=1:yyy(840)
    if ymicron(m) >= rin & ymicron(m) <=rout
        % Pulls the y_position in microns
        ypos(mm) = ymicron(m);
        % Pulls the Normalized Intensity
        Inormpos(mm) = ylinenorm(m);
        % Increments the counter
        mm=mm+1;
    end
end
% Takes natural log of Normalized Intensity
Ilnnormpos=log(Inormpos);
% Plots ln of Normalized Intensity vs. position
% Linear regression of plot, displays Diffusion Length, plots
regression
[P,S] = polyfit(ypos,Ilnnormpos,1);
```

```matlab
m=P(1);
Ldiff_0_pos=1/abs(m);
b=P(2);
f = @(y)m*y+b;
fplot(f,[rin rout]);
mm=1;
for m=1:yyy(840)
    if ymicron(m) <= -rin & ymicron(m) >= -rout
        % Pulls the y_position in microns
        yneg(mm) = ymicron(m);
        % Pulls the Normalized Intensity
        Inormneg(mm) = ylinenorm(m);
        % Increments the counter
        mm=mm+1;
    end
end
% Takes natural log of Normalized Intensity
Ilnnormneg=log(Inormneg);
% Plots ln of Normalized Intensity vs. position
% Linear regression of plot, displays Diffusion Length, plots
regression
[P,S] = polyfit(yneg,Ilnnormneg,1);
m=P(1);
Ldiff_0_neg=1/abs(m);
b=P(2);
f = @(y)m*y+b;
fplot(f,[-rin -rout]);
        M = [Cy C];
        R = [ymicron,ylinenorm];  %This is using the actual pixel
values
%                                 from improfile command
        picpos = n-t+400;
        picpos = picpos';
        N = [picpos, max(C)];
        Q = [Ldiff_0_pos Ldiff_0_neg];
        D = {M R N Q};
        [h w] = size(M);
        a(1:h, 1:w, n) = M;
        sw = w+1;
        [hR wR] = size(R);
        a(1:hR, sw:sw+1, n) = R;
        sw = sw+w;
        [hN wN] = size(N);
        a(1:hN, sw:sw+1, n) = N;
        sw = sw+2;
        [hQ wQ] = size(Q);
        a(1:hQ, sw:sw+1, n) = Q;
        test = a(:,:, n);
        z = n;
        Data = 'Data';
        zz = num2str(z);
        filename = strcat(Data,zz);
        xlswrite(filename,test,'sheet1','A1');
end
```

```matlab
%READDATA_HORIZONTAL_UPDATED.M
clear all
clc
startx = 0;
stopx = 441;
starty = 4000;
stopy = 8000;
CC = (0:440);
DD = (0:440);
EE = (0:440);
FF = (0:440);
GG = [CC;DD;EE;FF];
[h w] = size(GG);
figure(5)
axis([0 1000 0 842]);
test = zeros(351, 3);
test(:,1) = 1:351;
for i = 375:725
    z = i;
    Data = 'Data';
    zz = num2str(z);
    filename = strcat(Data,zz);
    A = xlsread(filename,'sheet1');
    B = A;
    C = B(1,5:8);
    X = 1:1:i-374+1;
    lx = i-374;
    test(lx, 2) = C(2);
    test(lx, 3) = C(3);
    test(lx, 4) = C(4);
    [s e w] = size(test);
    a(1:s, 1:e, 1:w, i) = test;
    test2 = a(:,:,:, i);
    z = 726;
    Data = 'Data';
    zz = num2str(z);
    filename = strcat(Data,zz);
    xlswrite(filename,test2,'sheet1','A1');
end
    h1 = plot(test(:,1),test(:,2),'.','MarkerEdgeColor','k',...
        'MarkerFaceColor','g','Markersize',14);hold on;
    ax1 = gca;
    set(ax1,'XColor','k','YColor','k');
    ax2 = axes('Position',get(ax1,'Position'),'XAxisLocation','top',...
        'YAxisLocation','right','Color','none','XColor','k',...
        'YColor','k');hold on;
%     h2 = plot(test(:,1),test(:,3),'.','MarkerEdgeColor','b',...
%         'MarkerFaceColor','b','Markersize',14,'parent',ax2);
    h3 = plot(test(:,1),test(:,4),'.','MarkerEdgeColor','r',...
        'MarkerFaceColor','r','Markersize',14,'parent',ax2);hold on;
```

87

```matlab
    set(get(ax1,'Xlabel'),'String','Point
Position','Color','k','FontSize',14);
    set(get(ax1,'Ylabel'),'String','Intensity (Arb
Units)','Color','k','FontSize',14);
    set(get(ax2, 'Ylabel'),'String','Ldiff','Color','k','FontSize',14);
    title('Data for Position 1 Line Scan 2 Slow Speed
2','FontSize',16);
    h4 = legend(ax1,'location','E');
    set(h4,'Color','w','string','Intensity');
    h5 = legend(ax2);
    h6 = legend(h5,'Ldiff Negative','location','SE');
    set(h6,'Color','w');
  grid on;
```

LIST OF REFERENCES

[1]   Renewables 2007 Global Status Report, Renewable Energy Policy Network for the 21st Century. http://www.ren21.net, Last Access: December 2008.

[2]   United States Department of Energy Annual Energy Review 2007, http://www.eia.doe.gov/emeu/aer/contents.html, Last Access: December 2008.

[3]   H. Scheer, *The Solar Economy, Renewable Energy for a Sustainable Global Future.* Earthscan/James and James 2004.

[4]   J. Plambeck, "Energy on a Planetary Basis", University of Alberta, July 1996.

[5]   V. Smil, "Energy at the Crossroads," presented at the Organization for Economic Co-operation, Paris, France, 2006.

[6]   N. Lewis, and D. Nocera, *Proceedings of the National Academy of Sciences* **103**, 15729 (2006).

[7]   K. Zweibel, J. Mason, and V. Fthanakis, *Scientific American Magazine*, **298**, 64 (2008).

[8]   J. E. Ayers and A. E. Ayers, *Digital Integrated Circuits: Analysis and Design, First Edition.* Taylor and Francis, Inc., 2003. http://www.en.wikipedia.org/wiki/Depletion_zone, Last Access: December 2008.

[9]   S. M. Sze, *Semiconductor Devices, Physics and Technology, Second Edition.* John Wiley and Sons, New Jersey, 2002.

[10]   S. O. Kasap, *Principles of Electron Materials and Devices, Third Edition.* John Wiley and Sons, New York, 2006.

[11]   D. Crisp, A. Pathareb, and R. C. Ewell, *Progress in Photovoltaics Research and Applications* **54**, 2 (2004). http://www.en.wikipedia.org/wiki/Multijuction_photovoltaic_cell, Last Access: December 2008.

[12]   E. F. Schubert, *Light-Emitting Diodes, Second Edition.* Cambridge University Press, 2006. http://www.en.wikipedia.org/wiki/Lattice_constant, Last Access: December 2008.

[13]   H. Karam, R. King, B. Cavicchi, D. Krut, J. Ermer, M. Haddad, L. Cai, D. Joslin, M. Takahashi, J. Eldredge, W. Nishikawa, D. Lillington, B. Keyes, and R. Ahrenkiel, *IEEE Transaction on Electron Devices* **46**, 10 (1999).

[14]   T. Mills, "Direct imaging of minority charge carrier transport in triple junction solar cell layers," M.S. thesis, Naval Postgraduate School, Monterey, CA, 2006.

[15]   S. Michael, "Space Power and Radiation Effects" Course Notes, Naval Postgraduate School, Monterey, CA, March 2006.

[16]   D. Hull, D. J. Bacon, *Introduction to Dislocations, Fourth Edition* (Elsevier Science 2001). http://www.en.wikipedia.org/wiki/Dislocations, Last Access: December 2008.

[17]   R. Reed-Hill, *Physical Metallurgy Principles Third Edition.* CL-Engineering, 1991.

[18]   D. Hull, and D. Bacon, *Introduction to Dislocations Fourth Edition.* Butterworth-Heinemann, United Kingdom, 2001.

[19]   B. Fischer and K. Bohm, *Journal of Applied Physics* **50**, 8 (1979).

[20]   B. Yacobi, and D. Holt, *Cathodoluminescence Microscopy of Inorganic Solids.* Plenum Press, New York, 1990.

[21]   R. Ahrenkiel and M. Lundstrom, *Minority Carriers in III-V Semiconductors: Physics and Applications Vol. 39.* Academic Press, Inc., San Diego, 1993.

[22]   New Semiconductor Materials: Characteristics and Properties. Ioffe Phssico-Technical Institute, St. Petersburg. http://www.ioffe.rssi.ru/SVU/NSM/Semicond, Last Access: December 2008.

[23]   M. Wu, Y. Su, C. Chang, and K. Cheng, *Journal of Applied Physics* **58**, 11 (1985).

[24]   C. Klein, *Journal of Applied Physics* **39**, 2029 (1968).

[25]   K. Kayana, and S. Okayama, *Journal of Applied Physics* **5**, 43 (1972).

[26]   S. Winchell, "Transport imaging in the one dimensional limit," M.S. thesis, Naval Postgraduate School, Monterey, CA, June 2006.

[27]   D. Luber, "Direct Imaging of Minority Charge Carrier Transport in Luminescent Semiconductors," M.S. thesis, Naval Postgraduate School, Monterey, CA, September 2005.

[28]   R. Ahrenkiel, *Solid State Electronics* **35**, 3 (1992).

[29]   S. Pizzini, M. Guzzi, E. Grilli, and G. Borionetti, *Journal of Applied Physics* **12**, 10131 (2000).

[30]   S. Tardon, *Quantitative Photoluminescence Studies in a-Si:H/c-Si Solar Cells*, Doctorate Dissertation, University of Oldenburg, Bilbao, Spain, February 1975.

[31]   M. Yang, M. Yamaguchi, T. Takamoto, E. Ikeda, H. Kurita, and M. Ohmori, *Solar Energy Materials and Solar Cells* **45**, 331 (1997).

[32]   P. Grivickas, "Optical Studies of Carrier Transport and Fundamental Absorption in 4H-SiC and Si", Laboratory of Material and Semiconductor Physics, Royal Institute of Technology, Stockholm, 2004.

[33]   R. King, D. Law, K. Edmondson, C. Fetzer, R. Sherif, G. Kinsey, D. Krut, H. Cotal, and N. Karam, "Photovoltaic Energy Conversion," in *Conference Record of the 2006 IEEE 4th World Conference,* 2006, pp. 760.

[34]   S. Cheng, *Superlattices and Microstructures* **33,** 1 (2003).

[35]   M. Dupuy, *Journal of Physics* **C4**, 44 (1983).

THIS PAGE INTENTIONALLY LEFT BLANK

INITIAL DISTRIBUTION LIST

1.   Defense Technical Information Center
        Ft. Belvoir, Virginia

2.   Dudley Knox Library
        Naval Postgraduate School
        Monterey, California

3.   Professor James H. Luscombe
        Naval Postgraduate School
        Monterey, California

4.   Professor Nancy M. Haegel
        Naval Postgraduate School
        Monterey, California

5.   Professor Clyde Scandrett
        Naval Postgraduate School
        Monterey, California

6.   Scott Edward Williams
        Bath, Maine